

Critical role of interlayer dimer correlations in the superconductivity of $\text{La}_3\text{Ni}_2\text{O}_7$

Siheon Ryee ^{1,*}, Niklas Witt ^{1,2} and Tim O. Wehling ^{1,2}

¹*Institute of Theoretical Physics, University of Hamburg, Notkestrasse 9, 22607 Hamburg, Germany*

²*The Hamburg Centre for Ultrafast Imaging, Luruper Chaussee 149, 22761 Hamburg, Germany*

(Dated: October 27, 2023)

The recent discovery of superconductivity in $\text{La}_3\text{Ni}_2\text{O}_7$ with $T_c \simeq 80\text{K}$ under high pressure opens up a new route to high- T_c superconductivity. This material realizes a bilayer square lattice model featuring a strong interlayer hybridization unlike many unconventional superconductors. A key question in this regard concerns how electronic correlations driven by the interlayer hybridization affect the low-energy electronic structure and the concomitant superconductivity. Here, we demonstrate using a cluster dynamical mean-field theory that the interlayer electronic correlations (IECs) induce a Lifshitz transition resulting in a change of Fermi surface topology. By solving an appropriate gap equation, we further show that the dominant pairing instability (intraorbital s -wave/interorbital $d_{x^2-y^2}$ -wave) is enhanced by the IECs. The underlying mechanism is the quenching of a strong ferromagnetic channel, resulting from the Lifshitz transition driven by the IECs. Our finding establishes the role of IECs in $\text{La}_3\text{Ni}_2\text{O}_7$ and potentially paves the way to designing higher- T_c nickelates.

The recent discovery of superconductivity in bilayer nickelate $\text{La}_3\text{Ni}_2\text{O}_7$ under high pressure [Fig. 1(a)] heralds a new class of high- T_c superconductors [1]. Without doping, this material exhibits superconductivity under pressure exceeding 14 GPa with maximal critical temperature of $T_c \simeq 80\text{K}$ [1–5]. Notable feature in $\text{La}_3\text{Ni}_2\text{O}_7$ is a multiorbital nature of low-lying states already at the level of density functional theory (DFT) [1, 6–20] [Fig. 1(b)]. Namely, three electrons per unit cell are distributed over Ni- e_g orbitals in the top and bottom square-planar lattices, whereas Ni- t_{2g} orbitals are fully occupied, thereby inactive for the low-energy physics. The two layers are coupled dominantly via interlayer nearest-neighbor hopping (or hybridization) between Ni- d_{z^2} orbitals ($t_{\perp}^z \simeq -0.63\text{eV}$) [6, 8, 13]. The hopping between Ni- $d_{x^2-y^2}$ is much smaller ($|t_{\perp}^x| < 0.05\text{eV}$) [6, 8]. Most importantly, t_{\perp}^z is deemed to be crucial for the noninteracting Fermi surface (FS) topology and theories of superconductivity in $\text{La}_3\text{Ni}_2\text{O}_7$ [12, 13, 16, 18, 19, 21–29].

In this respect, an important open question concerns how interlayer electronic correlations (IECs) driven by $t_{\perp}^{x/z}$ modify the low-energy electronic structure and how they affect superconductivity. Understanding the effects of $t_{\perp}^{x/z}$ would potentially enable us to design higher- T_c nickelates. Since t_{\perp}^z is the largest among all the hopping amplitudes [6, 8], one can identify the interlayer nearest-neighbor electronic correlations in the Ni- d_{z^2} states as the leading “nonlocal” correlations.

In this paper, we employ a cluster (cellular) dynamical mean-field theory (CDMFT) [30–32] to address nonperturbatively the nonlocal as well as the local electronic correlations within the two-site clusters (dimers) of the bilayer square lattice model for $\text{La}_3\text{Ni}_2\text{O}_7$ [Fig. 1(a)]. One of the key results of our study is a Lifshitz transition resulting in a change of the FS topology which does not occur when only local correlations are taken into account. By solving an appropriate gap equation using the dressed one-particle propagators obtained from CDMFT, we show that the IECs promote spin-singlet intraorbital s -wave/interorbital $d_{x^2-y^2}$ -wave pairing, namely the $s\pm$ -wave pairing. The underlying mechanism is the quenching of ferromagnetic (FM) fluctuations resulting

from the Lifshitz transition by IECs.

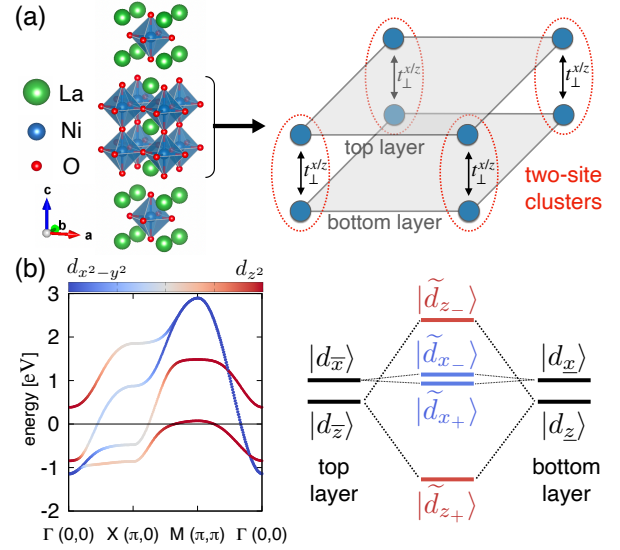


FIG. 1. (a) Left: Crystal structure of $\text{La}_3\text{Ni}_2\text{O}_7$ under high pressure drawn using VESTA [33]. Right: The bilayer square lattice model for $\text{La}_3\text{Ni}_2\text{O}_7$. Two-site clusters (dimers) consisting of top and bottom layer Ni sites (blue circles) coupled via $t_{\perp}^{x/z}$ are highlighted with red-dotted ovals. (b) Left: MLWF bands of the DFT electronic structure. The colorbar indicates the orbital character. Right: Sketch of the formation of four BA orbitals within the dimer consisting of the Ni- e_g orbitals in the top and bottom layers.

We consider a Hamiltonian on the bilayer square lattice: $\mathcal{H} = H_0 + H_{\text{int}}$. Here, H_0 is a tight-binding term describing the noninteracting band structure for which we use the maximally localized Wannier function (MLWF) description for the DFT result of $\text{La}_3\text{Ni}_2\text{O}_7$ under high pressure (29.5 GPa) [8] [Fig. 1(b)]. H_{int} is the local interaction term between Ni- e_g orbital electrons on the same Ni site, and is given by the standard Kanamori form consisting of U (intraorbital Coulomb interaction), J (Hund’s coupling), and U' (interorbital Coulomb interaction; $U' = U - 2J$). We use $U = 3.7\text{eV}$, $J = 0.6\text{eV}$, and $U' = 2.5\text{eV}$ by taking *ab initio* estimates for the e_g

MLWF model [34]. See Supplemental Material for more information [35].

The impurity problem for CDMFT is solved using the hybridization-expansion continuous-time quantum Monte Carlo method [36, 37]. We investigate the system at temperature of $T = 1/145$ eV $\simeq 80$ K corresponding to the maximum experimental T_c [1]. To mitigate the Monte Carlo sign problem resulting from the large interlayer hybridization, we solve the model in a bonding-antibonding (BA) basis defined as the symmetric (+) and antisymmetric (−) combinations of the top and bottom layer e_g orbitals:

$$|\tilde{d}_{i\eta\pm\sigma}\rangle = (|d_{i\bar{\eta}\sigma}\rangle \pm |d_{i\eta\sigma}\rangle)/\sqrt{2}. \quad (1)$$

Here, ket symbols indicate the corresponding Wannier states with site index i for the bilayer square lattice and spin $\sigma \in \{\uparrow, \downarrow\}$. $\bar{\eta}$ and η represent Ni- e_g orbitals ($\eta \in \{x^2 - y^2, z^2\}$) in the top and bottom layers, respectively. We hereafter simply denote $x^2 - y^2$ by x and z^2 by z , and omit site and spin indices unless needed. Under this basis transformation, the Weiss mean field for the impurity problem and the resulting self-energy become orbital-diagonal. The interlayer hopping t_{\perp}^{η} between e_g orbitals $|d_{\bar{\eta}}\rangle$ and $|d_{\eta}\rangle$ turns into a hybridization gap of $2|t_{\perp}^{\eta}|$ between BA orbitals $|\tilde{d}_{\eta+}\rangle$ and $|\tilde{d}_{\eta-}\rangle$. Thus a small (large) splitting is realized for $\eta = x$ ($\eta = z$) [schematically shown in the right panel of Fig. 1(b)].

We first investigate how interlayer correlations affect the low-energy electronic structure by contrasting DMFT (in which all the nonlocal correlations are neglected [38]) and CDMFT results. We note that, in a reasonable range around the *ab initio* interaction parameters, neither Mott transitions nor a bad metal behavior emerge within our calculations; see Supplemental Material [35]. Thus, unlike cuprates and infinite-layer nickelates, the normal state of $\text{La}_3\text{Ni}_2\text{O}_7$ is a metal without forming unscreened local moments, which is in line with experiments [1–4].

Figure 2 presents the FSs obtained within DMFT and CDMFT. We find from the DMFT calculations that the local correlations alone do not affect the FS topology [Fig. 2(a)]. The size and the shape of three distinct FS pockets obtained from DFT, namely α , β , and γ pockets, remain intact. This result is also consistent with previous DFT+DMFT studies [7, 9, 24].

The IECs, however, significantly modify this picture [Fig. 2(b)]. While the α pocket remains nearly the same, the β and the γ pockets are largely affected by IECs. The β pocket becomes more “diamond-shaped” with spectral weight at the first Brillouin zone (FBZ) boundary being shifted toward the X point. This FS change has implications for the formation of spin and charge fluctuations pertinent to superconducting instabilities. We also find redistribution of electron occupations in favor of half-filled \bar{z} and \underline{z} orbitals with $\langle n \rangle_{\bar{z}} = \langle n \rangle_{\underline{z}} \simeq 0.93$ compared to the DMFT value of 0.85. Most interestingly, the γ pocket disappears which results in a Lifshitz transition of the FS leaving a vestige of its weight at the M point. Looking at the orbital character of the FS [left

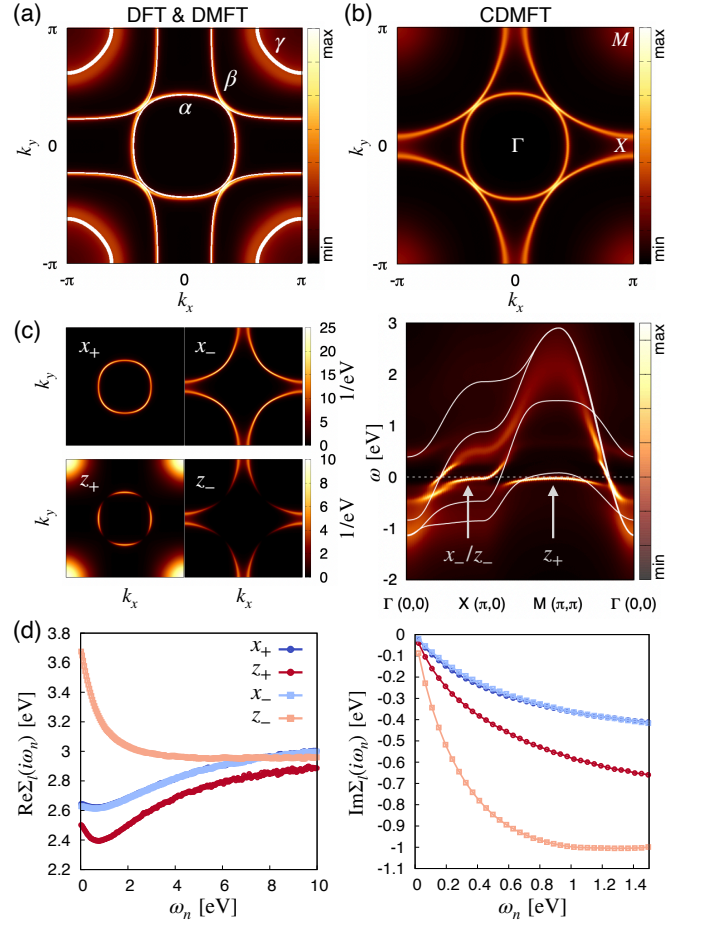


FIG. 2. (a) FSs obtained from the MLWF fit of DFT band structure (white lines) and DMFT (color map). (b) FS of the CDMFT. The FSs of DMFT and CDMFT in (a) and (b) are approximated to $-\sum_{lm} \delta_{lm} \Im G_{lm}(\mathbf{k}, i\omega_0)$ where $l, m \in \{x_+, z_+, x_-, z_-\}$. (c) Left panel: orbital character of the CDMFT FS. Right panel: the momentum-dependent spectral function obtained from CDMFT using the maximum entropy method [39, 40] (color map). The white solid lines indicate the DFT bands. The Fermi level is at $\omega = 0$. (d) The real and the imaginary parts of the CDMFT self-energy on the Matsubara frequency axis.

panel in Fig. 2(c)) reveals that x_- and z_- (for the β pocket around X point) and z_+ (for the γ pocket around the M point) BA orbitals underlie the FS modification.

More information can be obtained by analyzing the momentum-dependent spectral function from CDMFT [right panel in Fig. 2(c)]. We observe an overall narrowing of the spectral weight by electronic correlations compared to the DFT bands. The sharp peaks right at the Fermi level reflect the formation of quasiparticles which make up the coherent FS. Importantly, bands shifts are responsible for the change of the FS topology: Close to the X point, the second lowest band moves upward such that x_- and z_- states get closer to the Fermi level. The rather flat band of z_+ character at the M point, on the other hand, sinks below the Fermi level, leading to the disappearance of the γ -pocket.

To further pinpoint the microscopic role of IECs, we investigate the CDMFT self-energy $\Sigma_l(i\omega_n)$ where $\omega_n = (2n + 1)\pi/T$ is the fermionic Matsubara frequency with n being integer and $l \in \{x_+, z_+, x_-, z_-\}$ [Fig. 2(c)]. Without IECs, $\Sigma_{x_+}(i\omega_n) = \Sigma_{x_-}(i\omega_n)$ and $\Sigma_{z_+}(i\omega_n) = \Sigma_{z_-}(i\omega_n)$, so IECs are manifested by a difference of the self-energies between the BA orbitals. We first find that $\Sigma_{x_+}(i\omega_n) \simeq \Sigma_{x_-}(i\omega_n)$ over the entire frequency range due to small t_{\perp}^x which results in a weak (almost negligible) IECs as anticipated.

In contrast to the x_{\pm} components, large t_{\perp}^z gives rise to strong IECs in the z_{\pm} components. Indeed, an intriguing dichotomy between high-frequency and the low-frequency limits emerges as detailed below. We focus on the real part $\Re\Sigma_l(i\omega_n)$ which modifies the on-site energy level of the orbital l . Let us first look at the high-frequency limit ($\omega_n \rightarrow \infty$) in which only the Hartree-Fock self-energies survive. Since there is no Coulomb interaction between the two layers in our model, $\Re\Sigma_{z_-}(i\omega_{\infty}) = \Re\Sigma_{z_+}(i\omega_{\infty})$ holds analytically which is also confirmed by our numerical calculation [see the behavior of $\Re\Sigma_{z_{\pm}}(i\omega_{\infty})$ with increasing ω_n in Fig. 2(d)]. Furthermore, the difference between $\Re\Sigma_{x_{\pm}}(i\omega_{\infty})$ and $\Re\Sigma_{z_{\pm}}(i\omega_{\infty})$ is about 0.1 eV, so the Hartree-Fock correction to the DFT band structure is basically negligible.

In the low-frequency regime ($\omega_n \ll 10$ eV), however, $\Re\Sigma_{z_+}(i\omega_n)$ is smaller and $\Re\Sigma_{z_-}(i\omega_n)$ is noticeably larger than the value at the infinite frequency. This, in turn, shifts effectively the onsite energy levels of z_{\pm} upward (z_-) and downward (z_+) with respect to their DFT counterparts. From analytical continuation of the self-energies, the difference $\Re\Sigma_{z_-}(0) - \Re\Sigma_{z_+}(0)$ is found to be 1.17 eV, which implies an enhancement of the hybridization gap between z_+ and z_- by 1.17 eV due to IECs, or an “effective” interlayer hopping \tilde{t}_{\perp}^z of $|\tilde{t}_{\perp}^z| = |t_{\perp}^z| + 1.17$ eV. In fact, this low-energy behavior is the origin of the shifts of spectral weight and concomitant FS change seen in Fig. 2(b). Although x_- dominates over z_- in the spectral weight of the β pocket near the X point, a relatively weak downturn of $\Re\Sigma_{x_-}(i\omega_n)$ in the low-frequency regime is cancelled out by the large upturn of $\Re\Sigma_{z_-}(i\omega_n)$; this leads to the upward shift of the β pocket.

The physics observed here bears a close resemblance to that of VO₂ in which nonlocal correlations within dimers promote the formation of intradimer singlets with an enhanced hybridization gap à la the Heitler-London state of the Hubbard dimer [41–43]. Furthermore, since this interlayer hopping is relevant to the pairing mechanisms of La₃Ni₂O₇ [12, 13, 16, 18, 21–23, 26–29], our finding already highlights the importance of IECs in understanding the superconductivity.

Let us now turn to the imaginary part of the CDMFT self-energy, $\Im\Sigma_l(i\omega_n)$ [Fig. 2(d)]. Noticeable is the strongly orbital-dependent $\Im\Sigma_l(i\omega_n)$: the z_{\pm} components are more correlated than the x_{\pm} , i.e., $|\Im\Sigma_{z_{\pm}}(i\omega_n)| > |\Im\Sigma_{x_{\pm}}(i\omega_n)|$. The result is qualitatively consistent with the available experimental data in the ambient-pressure structure of La₃Ni₂O₇ [44, 45]. The origin is traced back to the resulting electron occupation of the \bar{z} and \underline{z} orbitals ($\langle n \rangle_{\bar{z}} = \langle n \rangle_{\underline{z}} \simeq 0.93$) being

much closer to half filling than the \bar{x} and \underline{x} ($\langle n \rangle_{\bar{x}} = \langle n \rangle_{\underline{x}} \simeq 0.57$) [35]. The IECs between \bar{z} and \underline{z} orbitals further differentiate z_+ and z_- , namely $|\Im\Sigma_{z_-}(i\omega_n)| > |\Im\Sigma_{z_+}(i\omega_n)|$, leading to a larger mass enhancement m^*/m_{DFT} (m_{DFT} is the bare DFT mass) in the z_- component. The mass enhancements directly extracted from $\Im\Sigma_l(i\omega_n)$ using the fourth-order polynomial fitting [46–48] are $m^*/m_{\text{DFT}} \simeq 2.8$ for z_+ and 5.1 for z_- . On the other hand, $m^*/m_{\text{DFT}} \approx 2$ for both weaker-correlated x_+ and x_- orbitals. Since $\Im\Sigma_l(i\omega_n \rightarrow 0) \ll T$ for all the orbitals [Fig. 2(d)], the low-energy physics is governed by heavy quasiparticles whose lifetime exceeds the intrinsic time scale of thermal fluctuations.

Having analyzed the effects of IECs on the electronic structure, we below investigate how they affect superconductivity. In light of the reported signatures of spin and charge density waves in La₃Ni₂O₇ at ambient pressure [49–53], it may be natural to consider spin- or charge-fluctuation-mediated pairing. We have found the predominance of spin susceptibilities over charge susceptibilities in our model, so we below focus on the spin-fluctuation-based mechanism.

A phase transition to the superconducting state occurs when the corresponding pairing susceptibility diverges, which requires numerical evaluation of the pairing vertex $\Gamma^{\text{s/t}}$ for singlet (s) or triplet (t) Cooper pairs [54, 55] (bold symbols will be used to denote vectors and matrices). The spin and charge susceptibilities ($\chi^{\text{sp/ch}}$) and the related irreducible vertices of the corresponding channels ($\Gamma^{\text{sp/ch}}$) contribute to $\Gamma^{\text{s/t}}$ in the form of ladder diagrams. Calculating frequency- and momentum-dependent $\Gamma^{\text{sp/ch}}$ and $\chi^{\text{sp/ch}}$, however, is highly nontrivial for multiorbital systems. We thus follow an idea previously employed to study cuprates, ruthenates, and iron-based superconductors [56–59]. Namely, $\Gamma^{\text{sp/ch}}$ are parametrized by effective screened intraorbital Coulomb interaction \bar{U} and Hund’s coupling \bar{J} , i.e., $\Gamma^{\text{sp/ch}} \rightarrow \bar{\Gamma}^{\text{sp/ch}}(\bar{U}, \bar{J})$ (we assume the interorbital value $\bar{U}' = \bar{U} - 2\bar{J}$). The effective vertices $\bar{\Gamma}^{\text{sp/ch}}(\bar{U}, \bar{J})$ are independent of frequency and momentum, see Supplemental Material [35]. It leads to a gap equation

$$\lambda_{\text{sc}} \Delta_{lm}(k) = -\frac{T}{2N} \sum_{q, l_1 m_1 m_2} \Gamma_{l m_1 l_1 m}^{\text{s/t}}(q) \times G_{l_1 l_2}(k - q) G_{m_1 m_2}(q - k) \Delta_{l_2 m_2}(k - q), \quad (2)$$

where λ_{sc} is the eigenvalue, $G(k)$ the (C)DMFT Green’s function, and $\Delta(k)$ the gap function. $k \equiv (\mathbf{k}, i\omega_n)$ and $q \equiv (\mathbf{q}, i\nu_n)$ with \mathbf{k} and \mathbf{q} being the crystal momentum and $\nu_n = 2n\pi/T$ the bosonic Matsubara frequency. N indicates the number of \mathbf{k} in the FBZ. $\Gamma_{l m_1 l_1 m}^{\text{s/t}}(q = k - k')$ describe the particle-particle scattering of electrons in orbitals (l, m) with four-momenta ($k, -k$) to (l_1, m_1) with ($k', -k'$). The transition to the superconducting state is indicated by the maximum (leading) eigenvalue λ_{sc} reaching unity. Since $\bar{\Gamma}^{\text{sp/ch}}(\bar{U}, \bar{J})$ are more sparse in the original e_g basis than the BA basis, so are the resulting $\chi^{\text{sp/ch}}$ and $\Gamma^{\text{s/t}}$. We therefore discuss below our results in the e_g picture.

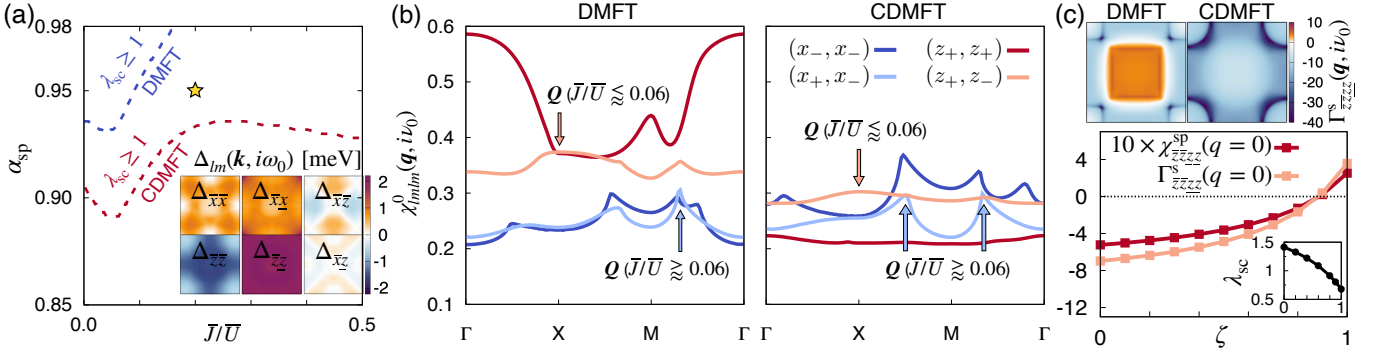


FIG. 3. (a) Superconducting phase diagram in the $\alpha_{\text{sp}} - \bar{J}/\bar{U}$ space at $T = 1/145$ eV $\simeq 80$ K. The superconductivity sets in (i.e., $\lambda_{\text{sc}} \geq 1$) in the regions above the dashed lines; blue for the DMFT and red for the CDMFT. Inset: the CDMFT gap functions in the FBZ for the parameter set marked by the yellow star which corresponds to $\alpha_{\text{sp}} = 0.95$ and $\bar{J}/\bar{U} = 0.2$. (b) The irreducible susceptibilities at the lowest bosonic frequency $\chi_{lm}^0(\mathbf{q}, i\nu_0)$ calculated using DMFT (left) and CDMFT (right) Green's functions. \mathbf{Q} and the associated $\chi^0(\mathbf{q}, i\nu_0)$ components are highlighted with colored arrows. (c) Upper panel: the spin-singlet pairing interaction $\Gamma_{\bar{z}\bar{z}z z}^{\text{SP}}(\mathbf{q}, i\nu_0)$ between top and bottom layer z orbitals in the FBZ. Lower panel: $\chi_{\bar{z}\bar{z}z z}^{\text{SP}}(q=0)$, $\Gamma_{\bar{z}\bar{z}z z}^{\text{S}}(q=0)$, and λ_{sc} (inset) as a function of scaling factor ζ for DMFT $\chi_{z_+z_+z_+z_+}^0(q)$. $\alpha_{\text{sp}} = 0.95$ and $\bar{J}/\bar{U} = 0.2$ for both panels.

We find the predominance of singlet over triplet pairings arising from antiferromagnetic (AFM) fluctuations. Figure 3(a) presents the resulting superconducting phase diagram for the leading singlet channel. Since we cannot pinpoint the precise magnitude of \bar{U} and \bar{J} , we scan a range of values. The vertical axis is given by the Stoner enhancement factor α_{sp} which indicates the maximum eigenvalue of $\bar{\Gamma}^{\text{SP}}(\bar{U}, \bar{J})\chi^0(\mathbf{q}, i\nu_0)$ and gauges the proximity to a magnetic instability. Here, χ^0 is the irreducible susceptibility, $\chi_{lm'l'm'}^0(q) = -\frac{T}{N} \sum_k G_{ll'}(k+q)G_{m'm}(k)$, which is the lowest-order term of the spin susceptibility, $\chi^{\text{SP}} = \chi^0[1 - \bar{\Gamma}^{\text{SP}}(\bar{U}, \bar{J})\chi^0]^{-1}$. Thus, α_{sp} is determined entirely from \bar{U} and \bar{J} , provided $\chi^0(\mathbf{q}, i\nu_0)$ is given [35]. For both DMFT and CDMFT cases, the leading pairing symmetry is always the intraorbital s -wave/interorbital $d_{x^2-y^2}$ -wave pairing in terms of the original e_g -orbital basis; see, for instance, the gap functions presented as the inset of Fig. 3(a). Transforming to the BA basis, this pairing corresponds to the “ s_{\pm} -wave” where the gap changes sign between BA orbitals in neighboring FS pockets. This leading pairing symmetry is in line with many previous studies [8, 12, 13, 18, 21–23, 25]. We note that the qualitative features of the gap functions remain unchanged over the entire parameter range while \mathbf{Q} (the crystal momentum at which the maximum eigenvalue of $\bar{\Gamma}^{\text{SP}}(\bar{U}, \bar{J})\chi^0(\mathbf{q}, i\nu_0)$ emerges) changes from $\mathbf{Q} = (\pi, 0)$ for $\bar{J}/\bar{U} \lesssim 0.06$ to an incommensurate wave vector around the M point for $\bar{J}/\bar{U} \gtrsim 0.06$ for both DMFT and CDMFT. See Fig. 3(b) for the related components of $\chi^0(\mathbf{q}, i\nu_0)$. In effect, kinks appearing in the phase boundaries at around $\bar{J}/\bar{U} \simeq 0.06$ are associated with this change.

The most notable feature of the phase diagram presented in Fig. 3(a) is the enhanced superconducting instabilities in the CDMFT compared to the DMFT over the entire range of parameters. This result is quite surprising because the γ pocket which disappears by IECs within our CDMFT calculation has

been argued to drive the spin-fluctuation-mediated superconductivity throughout the literature [9, 13, 16, 18, 21]. It thus raises the question: What is the role of the γ pocket in the pairing?

We first find that the γ pocket has a “Janus-faced” role: It hosts both obstructive and supportive magnetic fluctuations for the singlet pairing. This can be, in fact, traced back to the behavior of $\chi_{lm}^0(\mathbf{q}, i\nu_0)$ by investigating the $(l, m) = (z_+, z_+)$ and (z_+, z_-) components of the DMFT calculation in Fig. 3(b). While the γ pocket allows for small- \mathbf{q} particle-hole excitations resulting in the $\mathbf{q} = (0, 0)$ inter-layer FM fluctuation $\chi_{z_+z_+z_+z_+}^0(\mathbf{q}, i\nu_0)$, the $\mathbf{q} = (\pi, 0)$ nesting between the γ and β pocket gives rise to AFM fluctuation $\chi_{z_+z_-z_+z_-}^0(\mathbf{q}, i\nu_0)$. Thus, the γ pocket promotes two different competing (i.e., FM vs. AFM) magnetic channels. Importantly, however, the FM fluctuation predominates in DMFT as clearly shown in the left panel of Fig. 3(b).

The disappearance of the γ pocket from the FS due to IECs within CDMFT results in the suppression of both channels, especially the $\chi_{z_+z_+z_+z_+}^0$ -component involving solely the γ pocket [Fig. 3(b)]. This change is more apparent from the sign of the pairing interaction. In the singlet channel, the FM fluctuation is directly manifested by a repulsive (rather than attractive) interaction $\Gamma_{\bar{z}\bar{z}z z}^{\text{S}}(q=0)$ [upper panel of Fig. 3(c)], which hinders the s -wave singlet Cooper pairing between \bar{z} and z orbitals. Quenching of the FM $\chi_{z_+z_+z_+z_+}^0$ as in CDMFT yields the attractive pairing interaction $\Gamma_{\bar{z}\bar{z}z z}^{\text{S}}$ over the entire FBZ; see Fig. 3(c). Hence, the enhanced pairing tendency in CDMFT is mainly attributed to the suppression of this FM channel upon undergoing the Lifshitz transition.

To further corroborate this argument, we analyze how the DMFT superconducting instabilities are affected by the FM fluctuation by introducing a scaling factor ζ for $\chi_{z_+z_+z_+z_+}^0(q)$. Namely, $\chi_{z_+z_+z_+z_+}^0(q)$ is rescaled to $\zeta\chi_{z_+z_+z_+z_+}^0(q)$ before constructing $\chi^{\text{SP/ch}}$ and Γ^{S} . Indeed,

as shown in the lower panel of Fig. 3(c), the interlayer FM spin susceptibility $\chi_{zzzz}^{\text{sp}}(q=0)$ turns AFM with decreasing ζ followed by an attractive pairing interaction $\Gamma_{zzzz}^{\text{s}}(q=0)$ and an increase of λ_{sc} . See Supplemental Material for additional data [35].

To conclude, we have demonstrated that IECs play a critical role in the low-energy electronic structure of $\text{La}_3\text{Ni}_2\text{O}_7$ under high pressure by significantly modifying the FS topology and the resulting spin-susceptibility profile. The spin-fluctuation-mediated superconducting instabilities are found to be enhanced by IECs because they quench FM fluctuations due to an IEC-induced Lifshitz transition, whereby the γ pocket disappears. Our theory can be put to test, in principle, by measuring the FS and the spectral function with angle-resolved photoemission spectroscopy (ARPES). However, since ARPES cannot be deployed under this high-pressure condition, it would be desirable to examine whether superconductivity emerges in (artificially designed) bilayer nickelates at ambient pressure having the same low-energy electronic properties as we have found for the pressurized $\text{La}_3\text{Ni}_2\text{O}_7$.

Acknowledgments. We are grateful to F. Lechermann for useful discussion. This work is supported by the Cluster of Excellence ‘CUI: Advanced Imaging of Matter’ of the Deutsche Forschungsgemeinschaft (DFG) - EXC 2056 - project ID 390715994, by DFG priority program SPP 2244 (WE 5342/5-1 project No. 422707584) and the DFG research unit FOR 5242 (WE 5342/7-1, project No. 449119662). Calculations were done on the supercomputer Lise at NHR@ZIB as part of the NHR infrastructure under the project hhp00056.

* sryee@physnet.uni-hamburg.de

- [1] H. Sun, M. Huo, X. Hu, J. Li, Z. Liu, Y. Han, L. Tang, Z. Mao, P. Yang, B. Wang, J. Cheng, D.-X. Yao, G.-M. Zhang, and M. Wang, *Nature* **621**, 493 (2023), number: 7979 Publisher: Nature Publishing Group.
- [2] J. Hou, P. T. Yang, Z. Y. Liu, J. Y. Li, P. F. Shan, L. Ma, G. Wang, N. N. Wang, H. Z. Guo, J. P. Sun, Y. Uwatoko, M. Wang, G.-M. Zhang, B. S. Wang, and J.-G. Cheng, *Emergence of high-temperature superconducting phase in the pressurized $\text{La}_3\text{Ni}_2\text{O}_7$ crystals* (2023), arXiv:2307.09865 [cond-mat].
- [3] Y. Zhang, D. Su, Y. Huang, H. Sun, M. Huo, Z. Shan, K. Ye, Z. Yang, R. Li, M. Smidman, M. Wang, L. Jiao, and H. Yuan, *High-temperature superconductivity with zero-resistance and strange metal behavior in $\text{La}_3\text{Ni}_2\text{O}_7$* (2023), arXiv:2307.14819 [cond-mat].
- [4] G. Wang, N. Wang, J. Hou, L. Ma, L. Shi, Z. Ren, Y. Gu, X. Shen, H. Ma, P. Yang, Z. Liu, H. Guo, J. Sun, G. Zhang, J. Yan, B. Wang, Y. Uwatoko, and J. Cheng, *Pressure-induced superconductivity in the $\text{La}_3\text{Ni}_2\text{O}_7$ polycrystalline samples* (2023), arXiv:2309.17378 [cond-mat].
- [5] M. Zhang, C. Pei, Q. Wang, Y. Zhao, C. Li, W. Cao, S. Zhu, J. Wu, and Y. Qi, *Effects of Pressure and Doping on Ruddlesden-Popper phases $\text{La}_{n+1}\text{NiO}_{3n+1}$* (2023), arXiv:2309.01651 [cond-mat].
- [6] Z. Luo, X. Hu, M. Wang, W. Wú, and D.-X. Yao, *Physical Review Letters* **131**, 126001 (2023), publisher: American Physical Society.
- [7] D. A. Shilenko and I. V. Leonov, *Physical Review B* **108**, 125105 (2023), publisher: American Physical Society.
- [8] Y. Gu, C. Le, Z. Yang, X. Wu, and J. Hu, *Effective model and pairing tendency in bilayer Ni-based superconductor $\text{La}_3\text{Ni}_2\text{O}_7$* (2023), arXiv:2306.07275 [cond-mat].
- [9] F. Lechermann, J. Gondolf, S. Bötzel, and I. M. Eremin, *Electronic correlations and superconducting instability in $\text{La}_3\text{Ni}_2\text{O}_7$ under high pressure* (2023), arXiv:2306.05121 [cond-mat].
- [10] Y. Zhang, L.-F. Lin, A. Moreo, and E. Dagotto, *Electronic structure, orbital-selective behavior, and magnetic tendencies in the bilayer nickelate superconductor $\text{La}_3\text{Ni}_2\text{O}_7$ under pressure* (2023), arXiv:2306.03231 [cond-mat].
- [11] Y. Cao and Y.-f. Yang, *Flat bands promoted by Hund’s rule coupling in the candidate double-layer high-temperature superconductor $\text{La}_3\text{Ni}_2\text{O}_7$* (2023), arXiv:2307.06806 [cond-mat] version: 1.
- [12] Q.-G. Yang, D. Wang, and Q.-H. Wang, *Possible s_{\pm} -wave superconductivity in $\text{La}_3\text{Ni}_2\text{O}_7$* (2023), arXiv:2306.03706 [cond-mat].
- [13] H. Sakakibara, N. Kitamine, M. Ochi, and K. Kuroki, *Possible high T_c superconductivity in $\text{La}_3\text{Ni}_2\text{O}_7$ under high pressure through manifestation of a nearly-half-filled bilayer Hubbard model* (2023), arXiv:2306.06039 [cond-mat].
- [14] R. Jiang, J. Hou, Z. Fan, Z.-J. Lang, and W. Ku, *Pressure driven screening of Ni spin results in cuprate-like high- T_c superconductivity in $\text{La}_3\text{Ni}_2\text{O}_7$* (2023), arXiv:2308.11614 [cond-mat].
- [15] L. C. Rhodes and P. Wahl, *Structural routes to stabilise superconducting $\text{La}_3\text{Ni}_2\text{O}_7$ at ambient pressure* (2023), arXiv:2309.15745 [cond-mat].
- [16] Y. Zhang, L.-F. Lin, A. Moreo, T. A. Maier, and E. Dagotto, *Trends of electronic structures and s_{\pm} -wave pairing for the rare-earth series in bilayer nickelate superconductor $R_3\text{Ni}_2\text{O}_7$* (2023), arXiv:2308.07386 [cond-mat].
- [17] B. Geisler, J. J. Hamlin, G. R. Stewart, R. G. Hennig, and P. J. Hirschfeld, *Structural transitions, octahedral rotations, and electronic properties of $A_3\text{Ni}_2\text{O}_7$ rare-earth nickelates under high pressure* (2023), arXiv:2309.15078 [cond-mat].
- [18] Y.-B. Liu, J.-W. Mei, F. Ye, W.-Q. Chen, and F. Yang, *The s^{\pm} -Wave Pairing and the Destructive Role of Apical-Oxygen Deficiencies in $\text{La}_3\text{Ni}_2\text{O}_7$ Under Pressure* (2023), arXiv:2307.10144 [cond-mat].
- [19] H. LaBollita, V. Pardo, M. R. Norman, and A. S. Botana, *Electronic structure and magnetic properties of $\text{La}_3\text{Ni}_2\text{O}_7$ under pressure* (2023), arXiv:2309.17279 [cond-mat].
- [20] H. Sakakibara, M. Ochi, H. Nagata, Y. Ueki, H. Sakurai, R. Matsumoto, K. Terashima, K. Hirose, H. Ohta, M. Kato, Y. Takano, and K. Kuroki, *Theoretical analysis on the possibility of superconductivity in a trilayer Ruddlesden-Popper nickelate $\text{La}_4\text{Ni}_3\text{O}_{10}$ under pressure and its experimental examination: comparison with $\text{La}_3\text{Ni}_2\text{O}_7$* (2023), arXiv:2309.09462 [cond-mat].
- [21] Y. Zhang, L.-F. Lin, A. Moreo, T. A. Maier, and E. Dagotto, *Structural phase transition, s_{\pm} -wave pairing and magnetic stripe order in the bilayered nickelate superconductor $\text{La}_3\text{Ni}_2\text{O}_7$ under pressure* (2023), arXiv:2307.15276 [cond-mat].
- [22] H. Oh and Y.-H. Zhang, *Type II t-J model and shared antiferromagnetic spin coupling from Hund’s rule in superconducting $\text{La}_3\text{Ni}_2\text{O}_7$* (2023), arXiv:2307.15706 [cond-mat].
- [23] Z. Liao, L. Chen, G. Duan, Y. Wang, C. Liu, R. Yu, and Q. Si,

- Electron correlations and superconductivity in $\text{La}_3\text{Ni}_2\text{O}_7$ under pressure tuning (2023), arXiv:2307.16697 [cond-mat].
- [24] Q. Qin and Y.-f. Yang, **High- T_c superconductivity by mobilizing local spin singlets and possible route to higher T_c in pressurized $\text{La}_3\text{Ni}_2\text{O}_7$** (2023), arXiv:2308.09044 [cond-mat].
- [25] C. Lu, Z. Pan, F. Yang, and C. Wu, **Interlayer Coupling Driven High-Temperature Superconductivity in $\text{La}_3\text{Ni}_2\text{O}_7$ Under Pressure** (2023), arXiv:2307.14965 [cond-mat].
- [26] Y.-H. Tian, Y. Chen, J.-M. Wang, R.-Q. He, and Z.-Y. Lu, **Correlation Effects and Concomitant Two-Orbital s_{\pm} -Wave Superconductivity in $\text{La}_3\text{Ni}_2\text{O}_7$ under High Pressure** (2023), arXiv:2308.09698 [cond-mat].
- [27] D.-C. Lu, M. Li, Z.-Y. Zeng, W. Hou, J. Wang, F. Yang, and Y.-Z. You, **Superconductivity from Doping Symmetric Mass Generation Insulators: Application to $\text{La}_3\text{Ni}_2\text{O}_7$ under Pressure** (2023), arXiv:2308.11195 [cond-mat].
- [28] H. Lange, L. Homeier, E. Demler, U. Schollwöck, F. Grusdt, and A. Bohrdt, **Feshbach resonance in a strongly repulsive bilayer model: a possible scenario for bilayer nickelate superconductors** (2023), arXiv:2309.15843 [cond-mat].
- [29] W. Wú, Z. Luo, D.-X. Yao, and M. Wang, **Charge Transfer and Zhang-Rice Singlet Bands in the Nickelate Superconductor $\text{La}_3\text{Ni}_2\text{O}_7$ under Pressure** (2023), arXiv:2307.05662 [cond-mat].
- [30] A. I. Lichtenstein and M. I. Katsnelson, **Physical Review B** **62**, R9283 (2000).
- [31] G. Kotliar, S. Y. Savrasov, G. Pálsson, and G. Biroli, **Physical Review Letters** **87**, 186401 (2001), publisher: American Physical Society.
- [32] T. Maier, M. Jarrell, T. Pruschke, and M. H. Hettler, **Reviews of Modern Physics** **77**, 1027 (2005).
- [33] K. Momma and F. Izumi, **Journal of Applied Crystallography** **44**, 1272 (2011).
- [34] V. Christiansson, F. Petocchi, and P. Werner, **Correlated electronic structure of $\text{La}_3\text{Ni}_2\text{O}_7$ under pressure** (2023), arXiv:2306.07931 [cond-mat].
- [35] See Supplemental Material for additional data and discussion, which includes Refs. [8, 34, 36, 48, 54–76].
- [36] E. Gull, A. J. Millis, A. I. Lichtenstein, A. N. Rubtsov, M. Troyer, and P. Werner, **Rev. Mod. Phys.** **83**, 349 (2011).
- [37] C. Melnick, P. Sémon, K. Yu, N. D’Imperio, A.-M. Tremblay, and G. Kotliar, **Computer Physics Communications** **267**, 108075 (2021).
- [38] A. Georges, G. Kotliar, W. Krauth, and M. J. Rozenberg, **Rev. Mod. Phys.** **68**, 13 (1996).
- [39] M. Jarrell and J. Gubernatis, **Physics Reports** **269**, 133 (1996).
- [40] D. Bergeron and A.-M. S. Tremblay, **Phys. Rev. E** **94**, 023303 (2016).
- [41] S. Biermann, A. Poteryaev, A. I. Lichtenstein, and A. Georges, **Physical Review Letters** **94**, 026404 (2005), publisher: American Physical Society.
- [42] J. M. Tomczak, F. Aryasetiawan, and S. Biermann, **Physical Review B** **78**, 115103 (2008), publisher: American Physical Society.
- [43] W. Brito, M. Aguiar, K. Haule, and G. Kotliar, **Physical Review Letters** **117**, 056402 (2016), publisher: American Physical Society.
- [44] J. Yang, H. Sun, X. Hu, Y. Xie, T. Miao, H. Luo, H. Chen, B. Liang, W. Zhu, G. Qu, C.-Q. Chen, M. Huo, Y. Huang, S. Zhang, F. Zhang, F. Yang, Z. Wang, Q. Peng, H. Mao, G. Liu, Z. Xu, T. Qian, D.-X. Yao, M. Wang, L. Zhao, and X. J. Zhou, **Orbital-Dependent Electron Correlation in Double-Layer Nickelate $\text{La}_3\text{Ni}_2\text{O}_7$** (2023), arXiv:2309.01148 [cond-mat].
- [45] Z. Liu, M. Huo, J. Li, Q. Li, Y. Liu, Y. Dai, X. Zhou, J. Hao, Y. Lu, M. Wang, and H.-H. Wen, **Electronic correlations and energy gap in the bilayer nickelate $\text{La}_3\text{Ni}_2\text{O}_7$** (2023), arXiv:2307.02950 [cond-mat].
- [46] J. Mravlje, M. Aichhorn, T. Miyake, K. Haule, G. Kotliar, and A. Georges, **Physical Review Letters** **106**, 096401 (2011), publisher: American Physical Society.
- [47] S. Ryee, M. J. Han, and S. Choi, **Physical Review Letters** **126**, 206401 (2021), publisher: American Physical Society.
- [48] S. Ryee, S. Choi, and M. J. Han, **Physical Review Research** **5**, 033134 (2023), publisher: American Physical Society.
- [49] Z. Zhang, M. Greenblatt, and J. B. Goodenough, **Journal of Solid State Chemistry** **108**, 402 (1994).
- [50] S. Taniguchi, T. Nishikawa, Y. Yasui, Y. Kobayashi, J. Takeda, S.-i. Shamoto, and M. Sato, **Journal of the Physical Society of Japan** **64**, 1644 (1995), publisher: The Physical Society of Japan.
- [51] G. Wu, J. J. Neumeier, and M. F. Hundley, **Physical Review B** **63**, 245120 (2001), publisher: American Physical Society.
- [52] C. D. Ling, D. N. Argyriou, G. Wu, and J. J. Neumeier, **Journal of Solid State Chemistry** **152**, 517 (2000).
- [53] Z. Liu, H. Sun, M. Huo, X. Ma, Y. Ji, E. Yi, L. Li, H. Liu, J. Yu, Z. Zhang, Z. Chen, F. Liang, H. Dong, H. Guo, D. Zhong, B. Shen, S. Li, and M. Wang, **Science China Physics, Mechanics & Astronomy** **66**, 217411 (2022).
- [54] N. E. Bickers, in **Theoretical Methods for Strongly Correlated Electrons**, CRM Series in Mathematical Physics, edited by D. Sénéchal, A.-M. Tremblay, and C. Bourbonnais (Springer, New York, NY, 2004) pp. 237–296.
- [55] G. Rohringer, H. Hafermann, A. Toschi, A. Katanin, A. Antipov, M. Katsnelson, A. Lichtenstein, A. Rubtsov, and K. Held, **Reviews of Modern Physics** **90**, 025003 (2018), publisher: American Physical Society.
- [56] T. A. Maier, M. Jarrell, and D. J. Scalapino, **Physical Review B** **75**, 134519 (2007), publisher: American Physical Society.
- [57] R. Nourafkan, G. Kotliar, and A.-M. Tremblay, **Physical Review Letters** **117**, 137001 (2016), publisher: American Physical Society.
- [58] O. Gingras, R. Nourafkan, A.-M. S. Tremblay, and M. Côté, **Physical Review Letters** **123**, 217005 (2019), publisher: American Physical Society.
- [59] S. Käser, H. U. R. Strand, N. Wentzell, A. Georges, O. Parcollet, and P. Hansmann, **Physical Review B** **105**, 155101 (2022), publisher: American Physical Society.
- [60] T. Ayrál, S. Biermann, and P. Werner, **Physical Review B** **87**, 125149 (2013), publisher: American Physical Society.
- [61] M. Schüler, M. Rösner, T. O. Wehling, A. I. Lichtenstein, and M. I. Katsnelson, **Physical Review Letters** **111**, 036601 (2013), publisher: American Physical Society.
- [62] E. G. C. P. van Loon, M. Schüler, M. I. Katsnelson, and T. O. Wehling, **Physical Review B** **94**, 165141 (2016), publisher: American Physical Society.
- [63] F. Nilsson, L. Boehnke, P. Werner, and F. Aryasetiawan, **Physical Review Materials** **1**, 043803 (2017), publisher: American Physical Society.
- [64] S. Ryee, P. Sémon, M. J. Han, and S. Choi, **npj Quantum Materials** **5**, 1 (2020), number: 1 Publisher: Nature Publishing Group.
- [65] A. H. Nevidomskyy and P. Coleman, **Physical Review Letters** **103**, 147205 (2009), publisher: American Physical Society.
- [66] Z. P. Yin, K. Haule, and G. Kotliar, **Physical Review B** **86**, 195141 (2012), publisher: American Physical Society.
- [67] A. Georges, L. d. Medici, and J. Mravlje, **Annual Review of Condensed Matter Physics** **4**, 137 (2013).
- [68] C. Aron and G. Kotliar, **Physical Review B** **91**, 041110 (2015),

- publisher: American Physical Society.
- [69] S. Rye and T. O. Wehling, *Nano Letters* **23**, 573 (2023), <https://doi.org/10.1021/acs.nanolett.2c04169>.
- [70] J. Li, M. Wallerberger, N. Chikano, C.-N. Yeh, E. Gull, and H. Shinaoka, *Phys. Rev. B* **101**, 035144 (2020), [arxiv:1908.07575](https://arxiv.org/abs/1908.07575).
- [71] N. Witt, E. G. C. P. van Loon, T. Nomoto, R. Arita, and T. O. Wehling, *Physical Review B* **103**, 205148 (2021), publisher: American Physical Society.
- [72] N. Witt, J. M. Pizarro, J. Berges, T. Nomoto, R. Arita, and T. O. Wehling, *Physical Review B* **105**, L241109 (2022).
- [73] N. Witt, L. Si, J. M. Tomczak, K. Held, and T. Wehling, *No superconductivity in $\text{Pb}_9\text{Cu}_1(\text{PO}_4)_6\text{O}$ found in orbital and spin fluctuation exchange calculations* (2023), arXiv:2308.07261.
- [74] H. Shinaoka, J. Otsuki, M. Ohzeki, and K. Yoshimi, *Physical Review B* **96**, 035147 (2017).
- [75] H. Shinaoka, N. Chikano, E. Gull, J. Li, T. Nomoto, J. Otsuki, M. Wallerberger, T. Wang, and K. Yoshimi, *SciPost Physics Lecture Notes* **10.21468/scipostphyslectnotes.63** (2022).
- [76] M. Wallerberger, S. Badr, S. Hoshino, S. Huber, F. Kakizawa, T. Koretsune, Y. Nagai, K. Nogaki, T. Nomoto, H. Mori, J. Otsuki, S. Ozaki, T. Plaikner, R. Sakurai, C. Vogel, N. Witt, K. Yoshimi, and H. Shinaoka, *SoftwareX* **21**, 101266 (2023).

Supplemental Material for “Critical role of interlayer dimer correlations in the superconductivity of $\text{La}_3\text{Ni}_2\text{O}_7$ ”

Siheon Ryee ¹, Niklas Witt ^{1,2} and Tim O. Wehling ^{1,2}

¹*Institute of Theoretical Physics, University of Hamburg, Notkestrasse 9, 22607 Hamburg, Germany*

²*The Hamburg Centre for Ultrafast Imaging, Luruper Chaussee 149, 22761 Hamburg, Germany*

SM1. MICROSCOPIC MODEL

We consider a Hamiltonian on the bilayer square lattice: $\mathcal{H} = H_0 + H_{\text{int}}$. Here, H_0 is a tight-binding term describing the noninteracting band structure, which reads

$$H_0 = \sum_{il,jm,\sigma} t_{il,jm} d_{il\sigma}^\dagger d_{jm,\sigma}, \quad (\text{S1})$$

where $d_{il,\sigma}^\dagger$ ($d_{jm,\sigma}$) is the electron creation (annihilation) operator for site i, j of the bilayer square lattice, spin $\sigma \in \{\uparrow, \downarrow\}$, and orbital $l, m \in \{\bar{\eta}, \eta\}$ where $\bar{\eta}$ and η represent Ni- e_g orbitals $\eta \in \{x^2 - y^2, z^2\}$ in the top and bottom layers, respectively. We simply denote $x^2 - y^2$ by x and z^2 by z . $\{t_{il,jm}\}$ are the hopping amplitudes for which we use values obtained from the maximally localized Wannier function (MLWF) description of the DFT result for $\text{La}_3\text{Ni}_2\text{O}_7$ under high pressure (29.5 GPa) [S1]. Note in particular that $t_{\perp}^{\eta} \equiv t_{i\bar{\eta},i\eta} = t_{i\eta,i\bar{\eta}}$ with $t_{\perp}^x = -0.049$ eV and $t_{\perp}^z = -0.628$ eV [S1]. The band dispersion of H_0 is presented in Fig. 2(c) in the main text. H_{int} is the onsite interaction term given by the standard Kanamori form

$$H_{\text{int}} = \frac{1}{2} \sum_{i,lm'm'l',\sigma\sigma'} U_{lm'm'l'}^{\sigma\sigma'} d_{il\sigma}^\dagger d_{i'l'\sigma'}^\dagger d_{im'\sigma'} d_{im\sigma}, \quad (\text{S2})$$

where $l, l', m, m' \in \{\bar{x}, \bar{z}, x, z\}$. $U_{lm'm'l'}^{\sigma\sigma'}$ is nonzero only for $U \equiv U_{\bar{\eta}\bar{\eta}\bar{\eta}\bar{\eta}}^{\sigma\sigma} = U_{\bar{\eta}\bar{\eta}\bar{\eta}\bar{\eta}}^{\sigma-\sigma} = U_{\eta\eta\eta\eta}^{\sigma\sigma} = U_{\eta\eta\eta\eta}^{\sigma-\sigma}$, $U' \equiv U_{\bar{\eta}\bar{\eta}'\bar{\eta}\bar{\eta}'}^{\sigma\sigma} = U_{\eta\eta'\eta\eta'}^{\sigma-\sigma} = U_{\eta\eta'\eta\eta'}^{\sigma\sigma} = U_{\eta\eta'\eta\eta'}^{\sigma-\sigma}$, and $J \equiv U_{\bar{\eta}\bar{\eta}'\bar{\eta}'\bar{\eta}}^{\sigma\sigma} = U_{\bar{\eta}\bar{\eta}'\bar{\eta}'\bar{\eta}}^{\sigma-\sigma} = U_{\eta\eta'\eta'\eta}^{\sigma\sigma} = U_{\eta\eta'\eta'\eta}^{\sigma-\sigma} = U_{\eta\eta'\eta'\eta}^{\sigma\sigma} = U_{\eta\eta'\eta'\eta}^{\sigma-\sigma}$ ($\eta \neq \eta'$). We take $U = 3.7$, $J = 0.6$ eV, and $U' = U - 2J$ by taking *ab initio* estimates for the e_g MLWF model [S2].

To mitigate the Monte Carlo sign problem of the two-site cluster impurity, we solve the model in a bonding-antibonding (BA) basis in which the electron annihilation operator $\tilde{d}_{i\eta\pm\sigma}$ is defined as the symmetric (+) and antisymmetric (−) combinations of the top and bottom layer e_g orbital operators:

$$\begin{pmatrix} \tilde{d}_{ix+\sigma} \\ \tilde{d}_{iz+\sigma} \\ \tilde{d}_{ix-\sigma} \\ \tilde{d}_{iz-\sigma} \end{pmatrix} = \mathbf{A} \begin{pmatrix} d_{i\bar{x}\sigma} \\ d_{i\bar{z}\sigma} \\ d_{ix\sigma} \\ d_{iz\sigma} \end{pmatrix} = \frac{1}{\sqrt{2}} \begin{pmatrix} 1 & 0 & 1 & 0 \\ 0 & 1 & 0 & 1 \\ 1 & 0 & -1 & 0 \\ 0 & 1 & 0 & -1 \end{pmatrix} \begin{pmatrix} d_{i\bar{x}\sigma} \\ d_{i\bar{z}\sigma} \\ d_{ix\sigma} \\ d_{iz\sigma} \end{pmatrix}, \quad \text{where } \mathbf{A} = \frac{1}{\sqrt{2}} \begin{pmatrix} 1 & 0 & 1 & 0 \\ 0 & 1 & 0 & 1 \\ 1 & 0 & -1 & 0 \\ 0 & 1 & 0 & -1 \end{pmatrix}. \quad (\text{S3})$$

Under this basis transformation, H_0 and H_{int} are rewritten as

$$H_0 = \sum_{il,jm,\sigma} \left(\sum_{l_1,m_1} t_{il_1,jm_1} A_{l_1 l} A_{m_1 m}^* \right) \tilde{d}_{il\sigma}^\dagger \tilde{d}_{jm,\sigma}, \quad (\text{S4})$$

$$H_{\text{int}} = \frac{1}{2} \sum_{i,lm'm'l',\sigma\sigma'} \left(\sum_{l_1 m_2 m_1 l_2} U_{l_1 m_2 m_1 l_2}^{\sigma\sigma'} A_{l_1 l} A_{l_2 l'} A_{m_1 m}^* A_{m_2 m'}^* \right) \tilde{d}_{il\sigma}^\dagger \tilde{d}_{i'l'\sigma'}^\dagger \tilde{d}_{im'\sigma'} \tilde{d}_{im\sigma}. \quad (\text{S5})$$

The transformed Coulomb interaction tensor to the BA basis, namely $\tilde{U}_{lm'm'l'}^{\sigma\sigma'} = \sum_{l_1 m_2 m_1 l_2} U_{l_1 m_2 m_1 l_2}^{\sigma\sigma'} A_{l_1 l} A_{l_2 l'} A_{m_1 m}^* A_{m_2 m'}^*$, has in general nonzero four-index elements. While the four-index terms cause the Monte Carlo sign problem, it is actually largely alleviated in the BA basis compared to the e_g basis thanks to the orbital-diagonal hybridization function.

SM2. INFLUENCE OF DIFFERENT ONSITE INTERACTION PARAMETERS ON THE FERMI SURFACE

We have used *ab initio* estimate of U ($U = 3.7$ eV) and J ($J = 0.6$ eV) obtained from the constrained random phase approximation (cRPA) [S2] for our presentation in the main text. Since we have neglected i) frequency dependence of U and

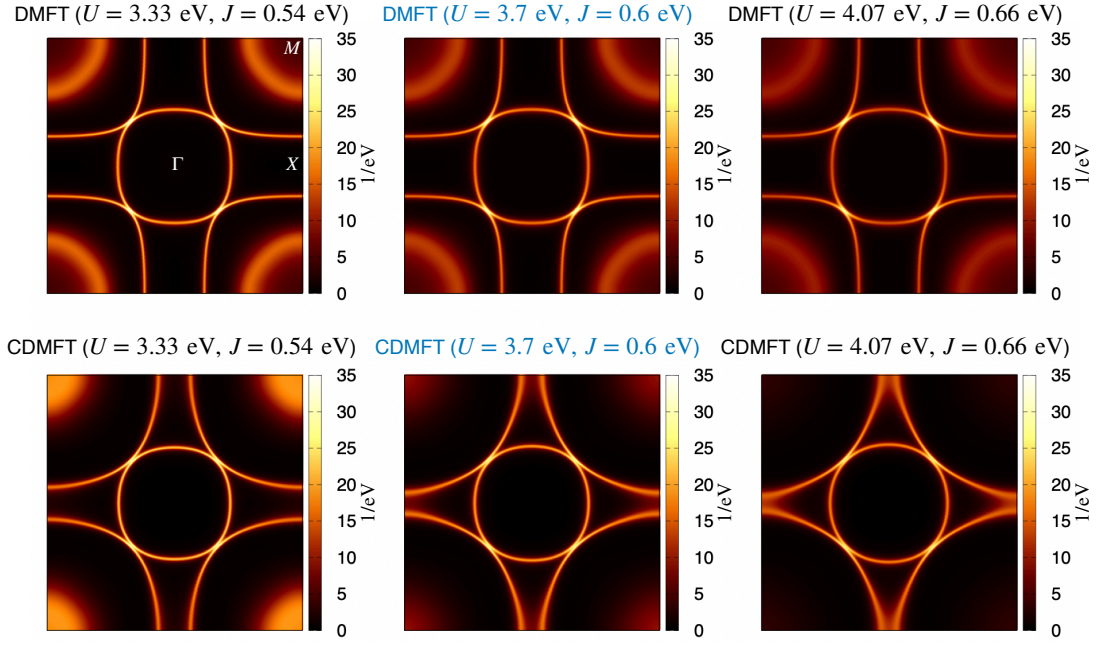


FIG. S1. The calculated FSs by DMFT (top panels) and CDMFT (bottom panel) for different interaction parameters. The FSs are approximated to $-\sum_{lm} \delta_{lm} \Im G_{lm}(\mathbf{k}, i\omega_0)$ where $l, m \in \{x_+, z_+, x_-, z_-\}$. The FSs in the middle panels are obtained from the *ab initio* interaction parameters. $U' = U - 2J$ for all the sets.

J by using their static limits and ii) spatially long-ranged Coulomb tails by taking only onsite values, it would be necessary to check how the low-energy electronic structure is affected by different values of U and J .

We present the calculated FSs in Fig. S1. As is expected, the strength of IECs increases with U and J . Namely, the γ pocket at the M point gets suppressed and the β pocket becomes more diamond-shaped with increasing U and J in CDMFT results. On the other hand, we find no appreciable change within DMFT in which only onsite electronic correlations are taken into account. In any case, we find that in a reasonable range around the cRPA estimates IECs significantly modify the FS making the γ pocket largely suppressed.

SM3. INFLUENCE OF INTERLAYER DENSITY-DENSITY INTERACTION V

Using the BA basis for CDMFT calculations, the nearest-neighbor interlayer interactions can be addressed on the same footing as onsite interactions (U and J) without invoking further computational complexity. In light of this, we here consider the effects of density-density interaction V within CDMFT by introducing an additional term H_V to our Hamiltonian. H_V reads

$$\begin{aligned}
 H_V &= \sum_{\eta, \eta' \in \{x, z\}}^{i\sigma\sigma'} V d_{i\eta\sigma}^\dagger d_{i\eta'\sigma'}^\dagger d_{i\eta'\sigma'} d_{i\eta\sigma} \quad (e_g \text{ basis}) \\
 &= \sum_{l, m \in \{x_+, z_+, x_-, z_-\}}^{i\sigma\sigma'} \left(\sum_{\eta, \eta' \in \{x, z\}} V A_{\eta l} A_{\eta' m} A_{\eta l}^* A_{\eta' m}^* \right) \tilde{d}_{il\sigma}^\dagger \tilde{d}_{im\sigma'}^\dagger \tilde{d}_{im\sigma'} \tilde{d}_{il\sigma} \quad (\text{BA basis}).
 \end{aligned} \tag{S6}$$

We use the cRPA estimate of V : $V = 0.5$ eV [S2].

Figure S2 presents the FS and the self-energy calculated by CDMFT with $V = 0.5$ eV. For comparison, we also show the results with $V = 0$. We first find that the FS is basically unaffected by V , although V slightly suppresses the γ pocket at the M point. This minor difference can be traced back to the small difference in the real part of the self-energy [upper panels in Fig. S2(b)]. For all orbital characters, the effect of V induces at most a ~ 0.1 eV decrease in the magnitude of the real part. Note that for comparison of the two cases on the same footing, we subtracted the infinite-frequency Hartree-Fock self-energy from the real part. We also find basically negligible modifications in the imaginary part of the self-energy [lower panels in Fig. S2(b)], albeit them being systematically decreased in magnitude by V . We can ascribe these suppressed real and imaginary parts of the self-energy in the finite V case to the generic effect of V which reduces the “effective” onsite interaction strength by screening

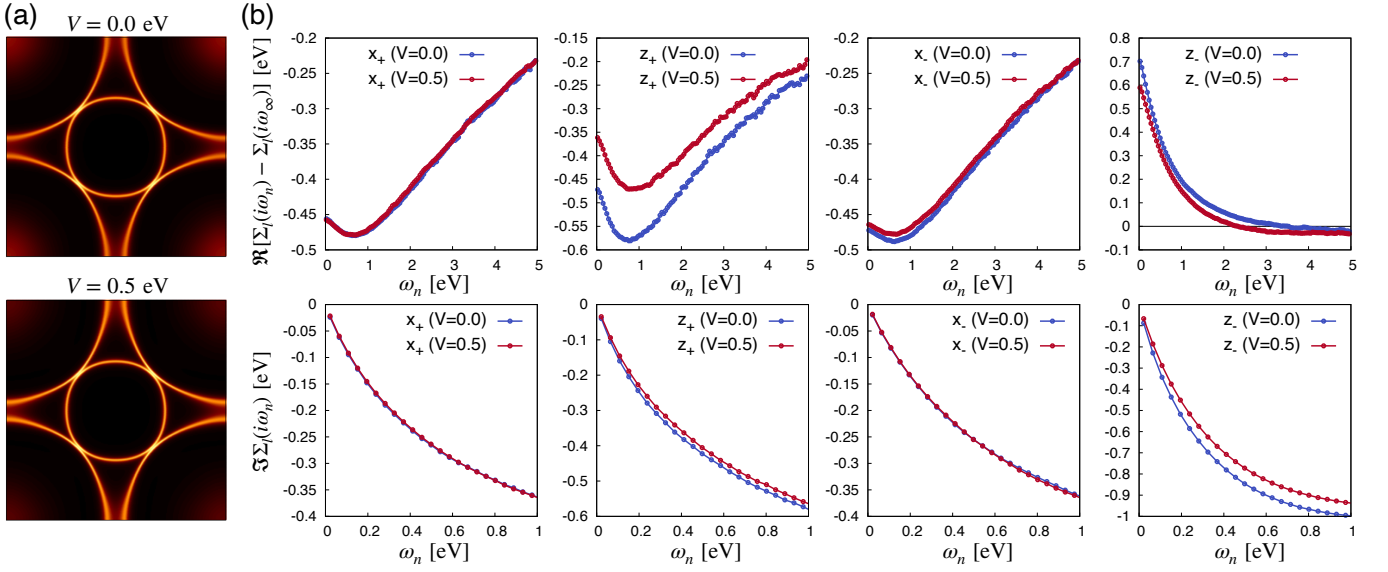


FIG. S2. (a) The calculated FSs by CDMFT for $V = 0$ (top) and $V = 0.5$ eV (bottom). (b) The real (top) and imaginary (bottom) parts of the CDMFT self-energies. $U = 3.7$ eV, $U = 0.6$ eV, and $U' = U - 2J = 2.5$ eV.

[S3–S7]. At any rate, these small changes in the FS and the self-energy legitimately allow us to employ only onsite interactions as we did in the present paper.

SM4. INFLUENCE OF HUND'S COUPLING J

Since $\text{La}_3\text{Ni}_2\text{O}_7$ realizes a multiorbital system, it would be informative to investigate how Hund's coupling J affects the low-energy physics. Figure S3 presents the effect of J on the imaginary part of the CDMFT self-energy. Interestingly, the magnitude of $\Im\Sigma_l(i\omega_n)$ increases for all the orbital character once we turn on J . Thus, the system becomes more correlated by J , which in this sense can be identified as a "Hund's metal" [S8]. This is because the formation of large local spin moments promoted by Hund's coupling suppresses Kondo screening, thereby prohibiting the emergence of long-lived quasiparticles [S8–S13]. We also find a strong orbital dependence of $\Im\Sigma_l(i\omega_n)$ for both $J = 0$ and $J = 0.6$ eV (the *ab initio* estimate) due to the fact that the electron occupation of the \bar{z} and \underline{z} orbitals is much closer to half filling than that of the \bar{x} and \underline{x} orbitals in both cases. The redistribution of electron filling by turning on J is found to be almost negligible in this system.

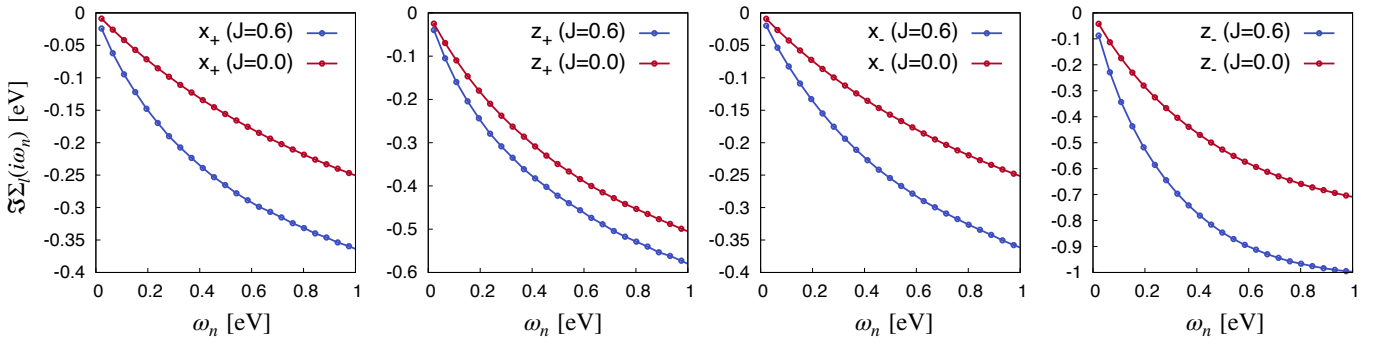


FIG. S3. The imaginary parts of the CDMFT self-energies for $J = 0.6$ eV (blue) and $J = 0.0$ eV (red). $U = 3.7$ eV and $U' = U - 2J$ for both cases.

SM5. GAP EQUATION

A. Pairing interactions

To obtain the effective singlet and triplet pairing interactions, we begin with the spin and charge irreducible vertices in the particle-hole channel, which read

$$\Gamma^{\text{sp/ch}}(q, k, k')_{l_1 l_2 l_3 l_4} = \Gamma_{\text{ph}}(q, k, k')_{l_1 l_2 l_3 l_4}^{\uparrow\uparrow\downarrow\downarrow} \mp \Gamma_{\text{ph}}(q, k, k')_{l_1 l_2 l_3 l_4}^{\uparrow\uparrow\uparrow\uparrow}. \quad (\text{S7})$$

$\Gamma_{\text{ph}}(q, k, k')_{l_1 l_2 l_3 l_4}^{\sigma_1 \sigma_2 \sigma_3 \sigma_4}$ is displayed in Fig. S4. $k \equiv (\mathbf{k}, i\omega_n)$ and $q \equiv (\mathbf{q}, i\nu_n)$. The spin and charge susceptibilities are obtained

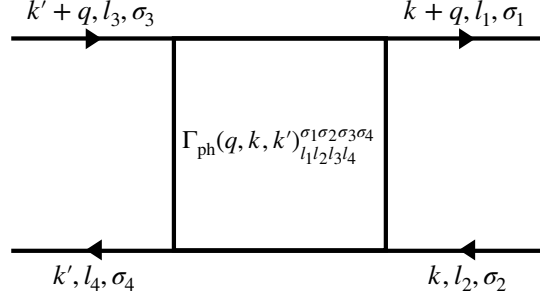


FIG. S4. The particle-hole irreducible vertex.

using these vertices from the Bethe-Salpeter equation:

$$\chi^{\text{sp/ch}}(q)_{kk'}^{l_1 l_2 l_7 l_8} = \chi^0(q)_{kk'}^{l_1 l_2 l_7 l_8} \pm \frac{T^2}{N^2} \chi^{\text{sp/ch}}(q)_{kk_1}^{l_1 l_2 l_3 l_4} \Gamma^{\text{sp/ch}}(q, k_1, k_2)_{l_3 l_4 l_5 l_6} \chi^0(q)_{k_2 k'}^{l_5 l_6 l_7 l_8}, \quad (\text{S8})$$

where $\chi^0(q)_{kk'}^{l_1 l_2 l_7 l_8} = -\frac{N}{T} G_{ll'}(k+q) G_{m'm}(k') \delta_{kk'}$. Here indices repeated twice should be summed over. We below keep this summation convention. By employing the parquet equations, one can formally express the singlet (s) and triplet (t) pairing interactions using $\Gamma^{\text{sp/ch}}$ and $\chi^{\text{sp/ch}}$ as [S14, S15]

$$\begin{aligned} \Gamma_{l_1 l_4 l_3 l_2}^s(k, k') &= \Lambda^{\text{irr},s}(k, k')_{l_1 l_4 l_3 l_2} + \frac{3}{2} \Phi^{\text{sp}}(-k+k', -k', k)_{l_2 l_4 l_3 l_1} - \frac{1}{2} \Phi^{\text{ch}}(-k+k', -k', k)_{l_2 l_4 l_3 l_1} \\ &\quad + \frac{3}{2} \Phi^{\text{sp}}(k+k', -k', -k)_{l_1 l_4 l_3 l_2} - \frac{1}{2} \Phi^{\text{ch}}(k+k', -k', -k)_{l_1 l_4 l_3 l_2}, \end{aligned} \quad (\text{S9})$$

$$\begin{aligned} \Gamma_{l_1 l_4 l_3 l_2}^t(k, k') &= \Lambda^{\text{irr},t}(k, k')_{l_1 l_4 l_3 l_2} - \frac{1}{2} \Phi^{\text{sp}}(-k+k', -k', k)_{l_2 l_4 l_3 l_1} - \frac{1}{2} \Phi^{\text{ch}}(-k+k', -k', k)_{l_2 l_4 l_3 l_1} \\ &\quad - \frac{1}{2} \Phi^{\text{sp}}(k+k', -k', -k)_{l_1 l_4 l_3 l_2} - \frac{1}{2} \Phi^{\text{ch}}(k+k', -k', -k)_{l_1 l_4 l_3 l_2}, \end{aligned} \quad (\text{S10})$$

where ladder vertices $\Phi^{\text{sp/ch}}(q, k, k')_{l_1 l_2 l_7 l_8} = \frac{T^2}{N^2} \Gamma^{\text{sp/ch}}(q, k, k_1)_{l_1 l_2 l_3 l_4} \chi^{\text{sp/ch}}(q)_{k_1 k_2}^{l_3 l_4 l_5 l_6} \Gamma^{\text{sp/ch}}(q, k_2, k')_{l_5 l_6 l_7 l_8}$. $\Lambda^{\text{irr},s/t}(k, k')_{l_1 l_4 l_3 l_2}$ are the fully irreducible vertices in the singlet (s) and triplet (t) channels. The bare constant terms of $\Lambda^{\text{irr},s/t}$, namely $\Lambda^{0,s/t}$, are linear combinations of bare spin and charge interaction tensors $\mathcal{U}^{\text{sp/ch}}$: $\Lambda_{l_1 l_4 l_3 l_2}^{0,s} = \frac{1}{2} [3\mathcal{U}^{\text{sp}} + \mathcal{U}^{\text{ch}}]_{l_1 l_4 l_3 l_2}$ and $\Lambda_{l_1 l_4 l_3 l_2}^{0,t} = -\frac{1}{2} [\mathcal{U}^{\text{sp}} - \mathcal{U}^{\text{ch}}]_{l_1 l_4 l_3 l_2}$. Since the interaction tensor H_{int} [Eq. (S2)] is more sparse in the original e_g -orbital basis than the BA basis, so are the resulting $\mathcal{U}^{\text{sp/ch}}$ which are given by $\mathcal{U}_{l_1 l_4 l_3 l_2}^{\text{sp/ch}} = \mathcal{U}_{l_1 l_3 l_4 l_2}^{\uparrow\downarrow} \mp (\mathcal{U}_{l_1 l_3 l_4 l_2}^{\uparrow\uparrow} - \mathcal{U}_{l_1 l_4 l_3 l_2}^{\uparrow\uparrow})$. In the e_g -orbital basis, elements of $\mathcal{U}^{\text{sp/ch}}$ read

$$\mathcal{U}_{l_1 l_4 l_3 l_2}^{\text{sp}} = \begin{cases} U \\ U' \\ J \\ J \end{cases}, \quad \mathcal{U}_{l_1 l_4 l_3 l_2}^{\text{ch}} = \begin{cases} U & \text{if } l_1 = l_2 = l_3 = l_4, \\ -U' + 2J & \text{if } l_1 = l_3 \neq l_2 = l_4, \\ 2U' - J & \text{if } l_1 = l_4 \neq l_2 = l_3, \\ J & \text{if } l_1 = l_2 \neq l_3 = l_4, \end{cases} \quad (\text{S11})$$

for the Kanamori interaction with $U' = U - 2J$. Using above formulas, a superconducting instability can be formulated in terms of a non-Hermitian eigenvalue problem, namely the gap equation, which reads

$$\lambda_{\text{sc}} \Delta_{l_1 l_2}(k) = -\frac{T}{2N} \sum_{k', l_3 l_4 l_5 l_6} \Gamma_{l_1 l_4 l_3 l_2}^{s/t}(k, k') G_{l_3 l_5}(k') G_{l_4 l_6}(-k') \Delta_{l_5 l_6}(k'), \quad (\text{S12})$$

where λ_{sc} is the eigenvalue, $G_{lm}(k)$ the (C)DMFT Green's function, and $\Delta_{lm}(k)$ the anomalous self-energy (gap function). The transition temperature T_c corresponds to the temperature at which the maximum (leading) eigenvalue λ_{sc} reaches unity.

B. Approximations for the pairing interactions and the resulting gap equation

Evaluating Eqs. (S9) and (S10) for the full vertex is a formidable task, it thus requires some approximations. First, we employ the well-known parquet approximation, which approximates $\Lambda^{\text{irr},s/t}$ by $\Lambda^{0,s/t}$. Within DMFT and CDMFT for our model, $\Gamma^{\text{sp/ch}}(q, k, k')_{l_1 l_2 l_3 l_4}$ can be approximated by the momentum-independent impurity vertices $\Gamma_{\text{imp}}^{\text{sp/ch}}(i\nu_m, i\omega_n, i\omega_{n'})_{l_1 l_2 l_3 l_4}$, which are in principle feasible to be numerically evaluated using the continuous-time quantum Monte Carlo methods [S16]. However, for multiorbital systems huge stochastic noise prohibits us from using the measured $\Gamma_{\text{imp}}^{\text{sp/ch}}(i\nu_m, i\omega_n, i\omega_{n'})_{l_1 l_2 l_3 l_4}$ in practice. Following an idea employed in Refs. [S17–S20], we parametrize $\Gamma^{\text{sp/ch}}$ using effective screened Coulomb interaction \bar{U} and Hund's coupling \bar{J} , i.e., we substitute $\Gamma^{\text{sp/ch}} \rightarrow \bar{\Gamma}^{\text{sp/ch}}(\bar{U}, \bar{J})$. As we used for the bare interaction, the effective screened interorbital Coulomb interaction \bar{U}' obeys $\bar{U}' = \bar{U} - 2\bar{J}$. Note that \bar{U} and \bar{J} are generally different from bare U and J which enter $\Lambda^{0,s/t}$. In the e_g -orbital basis, $\bar{\Gamma}^{\text{sp/ch}}(\bar{U}, \bar{J})$ are then given by

$$\bar{\Gamma}_{l_1 l_4 l_3 l_2}^{\text{sp}} = \begin{cases} \bar{U} \\ \bar{U}' \\ \bar{J} \\ \bar{J} \end{cases}, \quad \bar{\Gamma}_{l_1 l_4 l_3 l_2}^{\text{ch}} = \begin{cases} \bar{U} & \text{if } l_1 = l_2 = l_3 = l_4, \\ -\bar{U}' + 2\bar{J} & \text{if } l_1 = l_3 \neq l_2 = l_4, \\ 2\bar{U}' - \bar{J} & \text{if } l_1 = l_4 \neq l_2 = l_3, \\ \bar{J} & \text{if } l_1 = l_2 \neq l_3 = l_4, \end{cases} \quad (\text{S13})$$

Using this approximation,

$$\Phi^{\text{sp/ch}}(q, k, k')_{l_1 l_2 l_7 l_8} \rightarrow \bar{\Phi}^{\text{sp/ch}}(q)_{l_1 l_2 l_7 l_8} = \bar{\Gamma}_{l_1 l_2 l_3 l_4}^{\text{sp/ch}} \chi^{\text{sp/ch}}(q)_{l_3 l_4 l_5 l_6} \bar{\Gamma}_{l_5 l_6 l_7 l_8}^{\text{sp/ch}}. \quad (\text{S14})$$

Here $\chi^{\text{sp/ch}}(q)_{l_1 l_2 l_3 l_4} \equiv \frac{T^2}{N^2} \sum_{kk'} \chi^{\text{sp/ch}}(q)_{kk'}^{l_1 l_2 l_3 l_4}$ obtained from using $\bar{\Gamma}^{\text{sp/ch}}(\bar{U}, \bar{J})$ for the irreducible vertices in Eq. (S8):

$$\begin{aligned} \chi^{\text{sp/ch}}(q)_{l_1 l_2 l_3 l_4} &\equiv \frac{T^2}{N^2} \sum_{kk'} \chi^{\text{sp/ch}}(q)_{kk'}^{l_1 l_2 l_3 l_4} = \chi^0(q)_{l_1 l_2 l_7 l_8} \pm \chi^{\text{sp/ch}}(q)_{l_1 l_2 l_3 l_4} \bar{\Gamma}_{l_3 l_4 l_5 l_6}^{\text{sp/ch}} \chi^0(q)_{l_5 l_6 l_7 l_8}, \\ &= [\chi^0(q) [\mathbb{1} \mp \bar{\Gamma}^{\text{sp/ch}} \chi^0(q)]^{-1}]_{l_1 l_2 l_3 l_4}, \end{aligned} \quad (\text{S15})$$

where $\chi^0(q)_{l_1 l_2 l_3 l_4} \equiv \frac{T^2}{N^2} \sum_{kk'} \chi^0(q)_{kk'}^{l_1 l_2 l_3 l_4} = -\frac{T}{N} \sum_k G_{l_1 l_3}(k+q) G_{l_4 l_2}(k)$ and $\mathbb{1}$ is identity matrix in orbital space. We finally arrive at the gap equation presented in the main text

$$\lambda_{\text{sc}} \Delta_{l_1 l_2}(k) = -\frac{T}{2N} \sum_{k', l_3 l_4 l_5 l_6} \Gamma_{l_1 l_4 l_3 l_2}^{s/t}(k-k') G_{l_3 l_5}(k') G_{l_4 l_6}(-k') \Delta_{l_5 l_6}(k'). \quad (\text{S16})$$

Using the symmetry relations of singlet and triplet gap functions [S19, S20] the effective singlet and triplet pairing interactions $\Gamma^{s/t}$ in Eq. (S16) are given by

$$\begin{aligned} \Gamma^s(k-k')_{l_1 l_4 l_3 l_2} &= \Lambda_{l_1 l_4 l_3 l_2}^{0,s} + 3\bar{\Phi}^{\text{sp}}(k-k')_{l_1 l_4 l_3 l_2} - \bar{\Phi}^{\text{ch}}(k-k')_{l_1 l_4 l_3 l_2}, \\ &= \Lambda_{l_1 l_4 l_3 l_2}^{0,s} + 3[\bar{\Gamma}^{\text{sp}} \chi^{\text{sp}}(k-k') \bar{\Gamma}^{\text{sp}}]_{l_1 l_4 l_3 l_2} - [\bar{\Gamma}^{\text{ch}} \chi^{\text{ch}}(k-k') \bar{\Gamma}^{\text{ch}}]_{l_1 l_4 l_3 l_2}, \end{aligned} \quad (\text{S17})$$

$$\begin{aligned} \Gamma^t(k-k')_{l_1 l_4 l_3 l_2} &= \Lambda_{l_1 l_4 l_3 l_2}^{0,t} - \bar{\Phi}^{\text{sp}}(k-k')_{l_1 l_4 l_3 l_2} - \bar{\Phi}^{\text{ch}}(k-k')_{l_1 l_4 l_3 l_2}, \\ &= \Lambda_{l_1 l_4 l_3 l_2}^{0,s} - [\bar{\Gamma}^{\text{sp}} \chi^{\text{sp}}(k-k') \bar{\Gamma}^{\text{sp}}]_{l_1 l_4 l_3 l_2} - [\bar{\Gamma}^{\text{ch}} \chi^{\text{ch}}(k-k') \bar{\Gamma}^{\text{ch}}]_{l_1 l_4 l_3 l_2}. \end{aligned} \quad (\text{S18})$$

C. Solving the gap equation using the intermediate representation basis

We solve the gap equation [Eq. (S16)] on a 96×96 k -mesh using the power iteration method. We converge up to a tolerance of $5 \cdot 10^{-5}$ for the eigenvalue λ_{sc} of the dominant gap function. In order to efficiently solve this self-consistent problem, we use the sparse-sampling approach [S21–S24] of the intermediate representation (IR) basis [S25, S26] and its python library `sparse-ir` [S27] for efficient data compression. To set up the IR basis functions, we use the IR basis parameter $\Lambda_{\text{IR}} =$

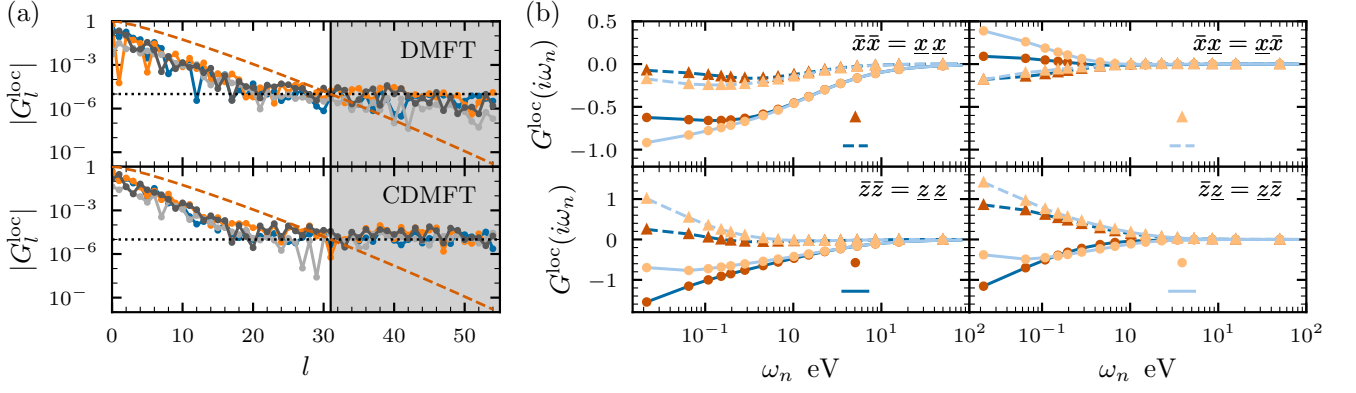


FIG. S5. Representation of local (C)DMFT Green's functions $G_l^{\text{loc}} = \frac{1}{N_{\mathbf{k}}} \sum_{\mathbf{k}} G_l(\mathbf{k})$ in the IR basis. (a) Expansion coefficients G_l as a function of expansion order l . Colored lines with dots correspond to coefficients for different orbital components in the e_g basis. The red dashed line corresponds to the truncation error set by the singular values. We cut the expansion after $l_{\text{max}} = 31$ coefficients (vertical solid line) with a truncation error of $\delta_{\text{IR}} = 10^{-5}$ (horizontal dotted line), such that the coefficients in the gray shaded area are disregarded. (b) Reconstruction of the (C)DMFT Green's function orbital components ($a, b \in \{\bar{x}, \bar{z}, \underline{x}, \underline{z}\}$) on a sparse frequency grid from the IR basis. Markers and lines represent data on the sparse IR grid and full equidistant grid, respectively. Note the logarithmic frequency axis.

$\beta\omega_{\text{max}} = 1450$ with inverse temperature $\beta = 145 \text{ eV}^{-1} \simeq 80 \text{ K}$ and cutoff frequency $\omega_{\text{max}} = 10 \text{ eV}$. We transform the (C)DMFT lattice Green's function $G(\mathbf{k}, i\omega_n) = [(i\omega_n + \mu)\mathbb{1} - H_0(\mathbf{k}) - \Sigma(i\omega_n)]^{-1}$ data ($\mathbb{1}$ is unity matrix in orbital space and μ the chemical potential) on its full and equidistantly sampled frequency mesh ($N_{\omega_n} = 1846$ for $\omega_n > 0$) to the IR basis functions U_l from the expansion

$$G(i\omega_n) = \sum_{l=0}^{l_{\text{max}}} G_l U_l(i\omega_n) \quad (\text{S19})$$

via least-square fitting. We set the truncation error to $\delta_{\text{IR}} = 10^{-5}$ to not overfit the statistical noise from the quantum Monte Carlo (QMC) simulations. This corresponds to using $N_{\text{IR}} = l_{\text{max}} - 1 = 31$ basis coefficients. Note, that we here use the notation ab instead of lm for orbital indices $\{\bar{x}, \bar{z}, \underline{x}, \underline{z}\}$ in the e_g basis to prevent confusion with the IR basis index l . We set the basis size from analyzing the decay of the local (C)DMFT Green's function expansion coefficients G_l^{loc} [Fig. S5(a)]. Beyond l_{max} (gray shaded area), the coefficients do not decay anymore and become larger than the exponentially decaying singular values S_l/S_0 (red dashed line) of the IR basis kernel due to fitting of QMC noise. The singular values approximately set the truncation error [S27]. By taking coefficients larger than the singular values into account, the conditioning of the transformation between IR basis and Matsubara frequency/imaginary time becomes bad, i.e., the numerical error can potentially amplify in an uncontrolled manner during calculation. Fig. S5(b) shows the corresponding reconstructed Green function data on a sparsely sampled frequency grid with $N_{\omega_n}^{\text{IR}} = l_{\text{max}} = 32$ frequency points.

SM6. MAPPING OF INTERACTION VALUES TO STONER ENHANCEMENT FACTORS

Throughout the paper, we discuss the superconducting phase diagram in terms of the Stoner enhancement factor α_{sp} . It is a proxy for the system's tendency towards a magnetic instability that we obtain from analyzing where the spin susceptibility χ^{sp} [Eq. (S15)] diverges, i.e., where the denominator becomes zero. This is true, if the largest eigenvalue $\alpha_{\text{sp}} = \max_q \{\bar{\Gamma}^{\text{sp}} \chi^0(q)\}$ reaches unity. Here, we comment further on the Stoner enhancement of the (C)DMFT calculations.

For a given $\chi^0(q)$, α_{sp} is a function of the effective Hund's coupling \bar{J} and the effective intraorbital Coulomb interaction \bar{U} . By fixing the value of \bar{J}/\bar{U} , the ratio $\alpha_{\text{sp}}/\bar{U}$ is uniquely determined, as we show in Fig. S6(a). This function exhibits a kink around $\bar{J}/\bar{U} \approx 0.05 - 0.06$ which is manifested as a kink in the superconducting phase boundary ($\lambda_{\text{sc}} = 1$) shown in Fig. 3(a) of the main text and Fig. (S8). The kink originates from two different wave vectors \mathbf{Q} at which the eigenvalue of $\bar{\Gamma}^{\text{sp}} \chi^0(\mathbf{Q}, i\nu_0)$ has its maximal value: around the X point $\mathbf{Q} \approx (\pi, 0)$ for $\bar{J}/\bar{U} \lesssim 0.06$ and an incommensurate wave vector around the M point for $\bar{J}/\bar{U} \gtrsim 0.06$ which we here denote by $\mathbf{Q} \approx (\kappa\pi, \kappa\pi)$ with $\kappa < 1$. The change between these two dominant momenta \mathbf{Q} depends on the momentum structure of $\chi^0(q)$ [c.f. Fig. 3(b) of the main text and Fig. S7 in Sec. SM7] and on how \bar{J} , \bar{U} mix different orbital components of $\chi^0(q)$. The exact location of the kink is, hence, different for the DMFT and CDMFT irreducible susceptibilities. It is noticeable that $\alpha_{\text{sp}}/\bar{U}$ of the DMFT calculation is generally larger than that of the CDMFT calculation.

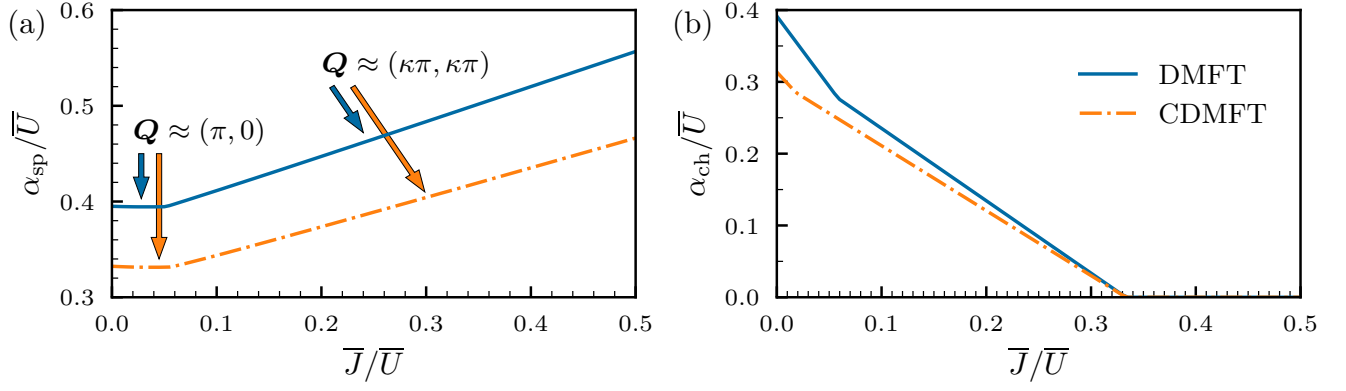


FIG. S6. Stoner enhancement factor in the (a) magnetic and (b) charge channel for the irreducible susceptibility of the (C)DMFT as a function of interaction ratio \bar{J}/\bar{U} . The kink around $\bar{J}/\bar{U} \approx 0.05-0.06$ originates from different \mathbf{Q} vectors contributing to the maximal eigenvalue of $\bar{\Gamma}^{\text{sp}}\chi^0(\mathbf{Q}, i\nu_0)$ as indicated by arrows.

For completeness, we mention that an identical analysis of possible charge instabilities can be made. Here, the charge Stoner enhancement $\alpha_{\text{ch}} = \max_q \{-\bar{\Gamma}^{\text{ch}}\chi^0(q)\}$ needs to be analyzed [Fig. S6(b)]. This system, however, does not host any charge instability because α_{ch} is too small.

SM7. ADDITIONAL DATA: STRUCTURE OF PAIRING VERTEX AND DOMINANT GAP FUNCTION

In the main text, we discuss the dominant pairing symmetry which is a singlet, intraorbital s -wave/interorbital $d_{x^2-y^2}$ -wave pairing in the original e_g -orbital basis or a s_{\pm} -wave symmetry in the BA basis. Apart from this symmetry, we checked many possible trial gap functions with different sign combinations of spin (S), parity (P), orbital (O), and time-reversal (T) symmetry which are in line with the D_{4h} symmetry of the model. Importantly, throughout the whole $\alpha_{\text{sp}} - \bar{J}/\bar{U}$ plane, none of these pairing channels have an eigenvalue larger than that of the s_{\pm} -wave symmetry. Only a subleading channel with intraorbital $d_{x^2-y^2}$ /interorbital s -wave pairing reaches for the CDMFT electronic structure an eigenvalue λ_{sc} of unity in the region of $\alpha_{\text{sp}} \gtrsim 0.96$ and $\bar{J}/\bar{U} \gtrsim 0.06$.

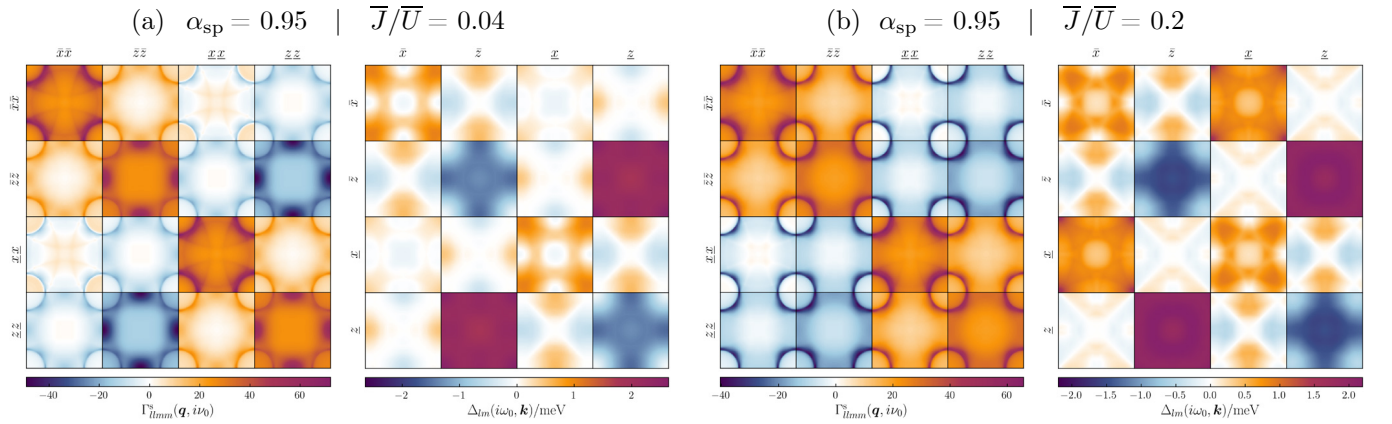


FIG. S7. Orbital and momentum space structure of the dominant singlet pairing vertex components $\Gamma_{llmm}^{\text{s}}(\mathbf{q}, i\nu_0)$ and singlet s_{\pm} -wave gap function $\Delta_{lm}(\mathbf{k}, i\omega_0)$ for $\alpha_{\text{sp}} = 0.95$ and two values of the interaction ratio $\bar{J}/\bar{U} = 0.04$ (a) and 0.2 (b). Note that the quantities are presented in the e_g -orbital basis.

Here, we discuss the full orbital and momentum structure of the dominant gap function $\Delta_{lm}(\mathbf{k}, i\omega_0)$ and dominant matrix elements of the singlet pairing vertex $\Gamma_{llmm}^{\text{s}}(\mathbf{q}, i\nu_0)$ obtained from the CDMFT electronic structure. We show those in Fig. S7 for $\bar{J}/\bar{U} = 0.04$ and 0.2 at $\alpha_{\text{sp}} = 0.95$ in the e_g -orbital basis. The vertex generally has an orbital block structure with intralayer components being positive and interlayer components being negative which originates from the interlayer AFM fluctuations.

The different dominant pairing vectors \mathbf{Q} discussed in the main text and in Sec. SM6 can be easily distinguished by comparing panels (a) and (b). However, increasing \bar{J}/\bar{U} does not only change the dominant \mathbf{Q} vector, but it also changes the relative weight of the orbital components. Namely, for small \bar{J}/\bar{U} mostly intraorbital components Γ_{lll}^s and the interlayer z components $\Gamma_{\bar{z}\bar{z}\bar{z}\bar{z}}^s$ play a role, whereas for larger \bar{J}/\bar{U} the magnitude of the components increases and evens out. This, in turn, affects the orbital structure of the dominant gap. By increasing \bar{J}/\bar{U} , the gap function gains more weight in the interlayer x -component $\Delta_{\bar{x}\bar{y}}$, i.e., the gap opening on the FS sheets with x_{\pm} character is enhanced.

SM8. ADDITIONAL DATA: THE CRITICAL ROLE OF FM $\chi_{z_+z_+z_+z_+}^0(q)$ IN THE SINGLET PAIRING

As we have discussed in the main text, the disappearance of the γ pocket from the FS due to IECs within CDMFT results leads to the suppression of the FM fluctuation arising from $\chi_{z_+z_+z_+z_+}^0(q, i\nu_0)$. In the singlet channel, this FM fluctuation is directly manifested by a repulsive (rather than attractive) interaction $\Gamma_{\bar{z}\bar{z}\bar{z}\bar{z}}^s(q=0)$. Quenching of the FM $\chi_{z_+z_+z_+z_+}^0$ as in CDMFT yields the attractive pairing interaction $\Gamma_{\bar{z}\bar{z}\bar{z}\bar{z}}^s(q=0)$ between top and bottom layer z orbitals as clearly shown in Fig. S8(b–d) for three distinct \bar{J}/\bar{U} values. This, in turn, promotes the singlet pairing as evidenced by the enhanced superconducting instabilities in CDMFT [Fig. S8(a)].

To further corroborate this argument, we analyze how the DMFT superconducting instabilities are affected by the FM fluctuation by introducing a scaling factor ζ for $\chi_{z_+z_+z_+z_+}^0(q)$. Namely, $\chi_{z_+z_+z_+z_+}^0(q)$ is rescaled to $\zeta\chi_{z_+z_+z_+z_+}^0(q)$ before constructing $\chi^{\text{sp/ch}}$ and Γ^s , and then we monitor how λ_{sc} behaves due to this change.

Interestingly, indeed, λ_{sc} increases with decreasing ζ for all the \bar{J}/\bar{U} values we investigated. Looking into the related spin susceptibilities, the components involving solely \bar{z} or z characters are found to be most affected by the rescaled $\chi_{z_+z_+z_+z_+}^0(q)$ as expected. In effect, as presented in Fig. S8(b–d), the interlayer FM spin susceptibility $\chi_{\bar{z}\bar{z}\bar{z}\bar{z}}^{\text{sp}}(q=0)$ at $\zeta=1$ becomes AFM with decreasing ζ . Through Eq. (S17) $\chi_{\bar{z}\bar{z}\bar{z}\bar{z}}^{\text{sp}}(q)$ directly affects the corresponding pairing interaction $\Gamma_{\bar{z}\bar{z}\bar{z}\bar{z}}^s(q)$, whereby it should faithfully follow the behavior of $\chi_{\bar{z}\bar{z}\bar{z}\bar{z}}^{\text{sp}}(q)$. As such, the repulsive pairing interaction $\Gamma_{\bar{z}\bar{z}\bar{z}\bar{z}}^s(q=0)$ at $\zeta=1$ turns attractive below $\zeta \simeq 0.9$ (for all the \bar{J}/\bar{U} values) at which $\chi_{\bar{z}\bar{z}\bar{z}\bar{z}}^{\text{sp}}(q=0)$ changes its sign; see orange lines in the lower panels of Fig. S8(b–d).

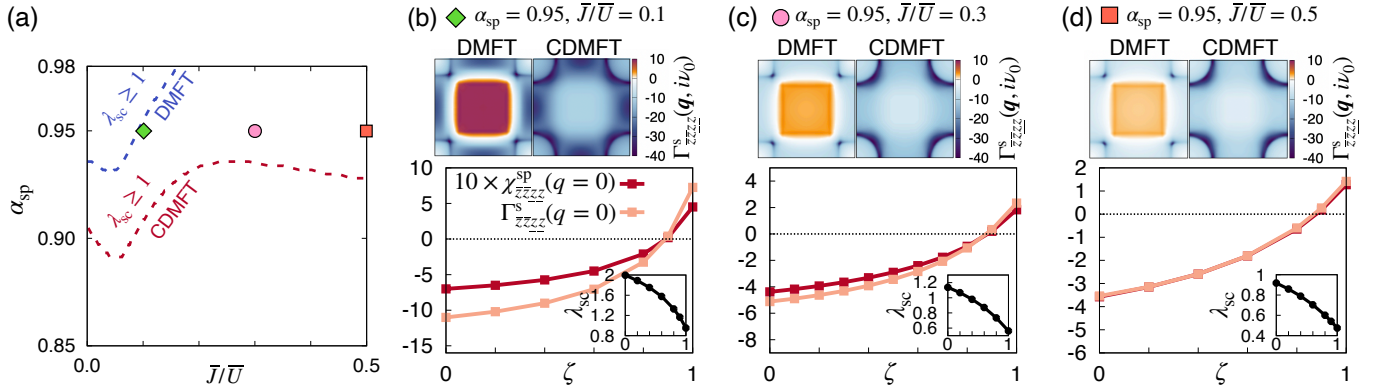


FIG. S8. (a) Superconducting phase diagram in the $\alpha_{\text{sp}} - \bar{J}/\bar{U}$ space at $T = 1/145$ eV $\simeq 80$ K. The superconductivity sets in (i.e., $\lambda_{\text{sc}} \geq 1$) in the regions above the dashed lines; blue for the DMFT and red for the CDMFT. (b–d) Upper panel: the spin-singlet pairing interaction $\Gamma_{\bar{z}\bar{z}\bar{z}\bar{z}}^s(q, i\nu_0)$ between top and bottom layer z orbitals in the FBZ. Lower panel: $\chi_{\bar{z}\bar{z}\bar{z}\bar{z}}^{\text{sp}}(q=0)$, $\Gamma_{\bar{z}\bar{z}\bar{z}\bar{z}}^s(q=0)$, and λ_{sc} (inset) as a function of scaling factor ζ for DMFT $\chi_{z_+z_+z_+z_+}^0(q)$.

- [S1] Y. Gu, C. Le, Z. Yang, X. Wu, and J. Hu, [Effective model and pairing tendency in bilayer Ni-based superconductor \$\text{La}_3\text{Ni}_2\text{O}_7\$](#) (2023), arXiv:2306.07275 [cond-mat].
- [S2] V. Christiansson, F. Petocchi, and P. Werner, [Correlated electronic structure of \$\text{La}_3\text{Ni}_2\text{O}_7\$ under pressure](#) (2023), arXiv:2306.07931 [cond-mat].
- [S3] T. Ayrál, S. Biermann, and P. Werner, [Physical Review B](#) **87**, 125149 (2013), publisher: American Physical Society.
- [S4] M. Schüler, M. Rösner, T. O. Wehling, A. I. Lichtenstein, and M. I. Katsnelson, [Physical Review Letters](#) **111**, 036601 (2013), publisher: American Physical Society.

- [S5] E. G. C. P. van Loon, M. Schüler, M. I. Katsnelson, and T. O. Wehling, *Physical Review B* **94**, 165141 (2016), publisher: American Physical Society.
- [S6] F. Nilsson, L. Boehnke, P. Werner, and F. Aryasetiawan, *Physical Review Materials* **1**, 043803 (2017), publisher: American Physical Society.
- [S7] S. Ryee, P. Sémon, M. J. Han, and S. Choi, *npj Quantum Materials* **5**, 1 (2020), number: 1 Publisher: Nature Publishing Group.
- [S8] A. Georges, L. d. Medici, and J. Mravlje, *Annual Review of Condensed Matter Physics* **4**, 137 (2013).
- [S9] A. H. Nevidomskyy and P. Coleman, *Physical Review Letters* **103**, 147205 (2009), publisher: American Physical Society.
- [S10] Z. P. Yin, K. Haule, and G. Kotliar, *Physical Review B* **86**, 195141 (2012), publisher: American Physical Society.
- [S11] C. Aron and G. Kotliar, *Physical Review B* **91**, 041110 (2015), publisher: American Physical Society.
- [S12] S. Ryee and T. O. Wehling, *Nano Letters* **23**, 573 (2023), <https://doi.org/10.1021/acs.nanolett.2c04169>.
- [S13] S. Ryee, S. Choi, and M. J. Han, *Physical Review Research* **5**, 033134 (2023), publisher: American Physical Society.
- [S14] N. E. Bickers, in *Theoretical Methods for Strongly Correlated Electrons*, CRM Series in Mathematical Physics, edited by D. Sénéchal, A.-M. Tremblay, and C. Bourbonnais (Springer, New York, NY, 2004) pp. 237–296.
- [S15] G. Rohringer, H. Hafermann, A. Toschi, A. Katanin, A. Antipov, M. Katsnelson, A. Lichtenstein, A. Rubtsov, and K. Held, *Reviews of Modern Physics* **90**, 025003 (2018), publisher: American Physical Society.
- [S16] E. Gull, A. J. Millis, A. I. Lichtenstein, A. N. Rubtsov, M. Troyer, and P. Werner, *Rev. Mod. Phys.* **83**, 349 (2011).
- [S17] T. A. Maier, M. Jarrell, and D. J. Scalapino, *Physical Review B* **75**, 134519 (2007), publisher: American Physical Society.
- [S18] R. Nourafkan, G. Kotliar, and A.-M. Tremblay, *Physical Review Letters* **117**, 137001 (2016), publisher: American Physical Society.
- [S19] O. Gingras, R. Nourafkan, A.-M. S. Tremblay, and M. Côté, *Physical Review Letters* **123**, 217005 (2019), publisher: American Physical Society.
- [S20] S. Käser, H. U. R. Strand, N. Wentzell, A. Georges, O. Parcollet, and P. Hansmann, *Physical Review B* **105**, 155101 (2022), publisher: American Physical Society.
- [S21] J. Li, M. Wallerberger, N. Chikano, C.-N. Yeh, E. Gull, and H. Shinaoka, *Phys. Rev. B* **101**, 035144 (2020), [arxiv:1908.07575](https://arxiv.org/abs/1908.07575).
- [S22] N. Witt, E. G. C. P. van Loon, T. Nomoto, R. Arita, and T. O. Wehling, *Physical Review B* **103**, 205148 (2021), publisher: American Physical Society.
- [S23] N. Witt, J. M. Pizarro, J. Berges, T. Nomoto, R. Arita, and T. O. Wehling, *Physical Review B* **105**, L241109 (2022).
- [S24] N. Witt, L. Si, J. M. Tomczak, K. Held, and T. Wehling, *No superconductivity in $\text{Pb}_9\text{Cu}_1(\text{PO}_4)_6\text{O}$ found in orbital and spin fluctuation exchange calculations* (2023), [arXiv:2308.07261](https://arxiv.org/abs/2308.07261).
- [S25] H. Shinaoka, J. Otsuki, M. Ohzeki, and K. Yoshimi, *Physical Review B* **96**, 035147 (2017).
- [S26] H. Shinaoka, N. Chikano, E. Gull, J. Li, T. Nomoto, J. Otsuki, M. Wallerberger, T. Wang, and K. Yoshimi, *SciPost Physics Lecture Notes* **10.21468/scipostphyslectnotes.63** (2022).
- [S27] M. Wallerberger, S. Badr, S. Hoshino, S. Huber, F. Kakizawa, T. Koretsune, Y. Nagai, K. Nogaki, T. Nomoto, H. Mori, J. Otsuki, S. Ozaki, T. Plaikner, R. Sakurai, C. Vogel, N. Witt, K. Yoshimi, and H. Shinaoka, *SoftwareX* **21**, 101266 (2023).